Constraining beyond the standard model nucleon isovector charges

R. E. Smail,[1] M. Batelaan,[1] R. Horsley,[2] Y. Nakamura,[3] H. Perlt,[4] D. Pleiter,[5] P. E. L. Rakow,[6] G. Schierholz,[7] H. Stüben,[8] R. D. Young,[1,9] and J. M. Zanotti[1]

(QCDSF/UKQCD/CSSM Collaboration)

[1]*CSSM, Department of Physics, University of Adelaide, Adelaide, South Australia 5005, Australia*
[2]*School of Physics and Astronomy, University of Edinburgh, Edinburgh EH9 3FD, United Kingdom*
[3]*RIKEN Center for Computational Science, Kobe, Hyogo 650-0047, Japan*
[4]*Institut für Theoretische Physik, Universität Leipzig, 04103 Leipzig, Germany*
[5]*PDC Center for High Performance Computing, KTH Royal Institute of Technology, SE-100 44 Stockholm, Sweden*
[6]*Theoretical Physics Division, Department of Mathematical Sciences, University of Liverpool, Liverpool L69 3BX, United Kingdom*
[7]*Deutsches Elektronen-Synchrotron DESY, Notkestraße 85, 22607 Hamburg, Germany*
[8]*Universität Hamburg, Regionales Rechenzentrum, 20146 Hamburg, Germany*
[9]*Center for Theoretical Physics, Massachusetts Institute of Technology, Cambridge, Massachusetts 02139, USA*

(Received 13 April 2023; accepted 13 October 2023; published 27 November 2023)

At the TeV scale, low-energy precision observations of neutron characteristics provide unique probes of novel physics. Precision studies of neutron decay observables are susceptible to beyond the Standard Model (BSM) tensor and scalar interactions, while the neutron electric dipole moment, d_n, also has high sensitivity to new BSM *CP*-violating interactions. To fully utilize the potential of future experimental neutron physics programs, matrix elements of appropriate low-energy effective operators within neutron states must be precisely calculated. We present results from the QCDSF/UKQCD/CSSM Collaboration for the isovector charges g_T, g_A and g_S of the nucleon, Σ and Ξ baryons using lattice QCD methods and the Feynman-Hellmann theorem. We use a flavor symmetry breaking method to systematically approach the physical quark mass using ensembles that span five lattice spacings and multiple volumes. We extend this existing flavor-breaking expansion to also account for lattice spacing and finite volume effects in order to quantify all systematic uncertainties. Our final estimates of the nucleon isovector charges are $g_T = 1.010(21)_{\text{stat}}(12)_{\text{sys}}$, $g_A = 1.253(63)_{\text{stat}}(41)_{\text{sys}}$ and $g_S = 1.08(21)_{\text{stat}}(03)_{\text{sys}}$ renormalized, where appropriate, at $\mu = 2$ GeV in the $\overline{\text{MS}}$ scheme.

DOI: 10.1103/PhysRevD.108.094511

I. INTRODUCTION

Historically nuclear and neutron beta decays have played an important role in determining the vector-axial (V-A) structure of weak interactions and in shaping the Standard Model (SM). However, more recently, neutron and nuclear β-decays can also be used to probe the existence of beyond the Standard Model (BSM) tensor and scalar interactions. The interaction of the W boson with the neutron and proton during neutron β-decay is proportional to the matrix element of flavor-changing vector and axial-vector currents between the initial neutron state and final proton state, with coupling constants $g_A/g_V = 1.2756(13)$ [1]. It has been identified that the potential existence of BSM tensor and scalar couplings would provide additional contributions to neutron β-decay [2]. These new BSM contributions are proportional to analogous matrix elements of flavor-changing tensor or scalar operators. To gain sensitivity to these effects the majority of previous and proposed neutron beta decay studies aim to determine one or more of the correlation coefficients included in the differential decay rate for a beam of polarized neutrons [2],

$$\frac{d^3\Gamma}{dE_e d\Omega_e \Omega_\nu} \propto p_e E_e (E_0 - E_e)^2 \xi \cdot \left(1 + a\frac{\mathbf{p}_e \cdot \mathbf{p}_\nu}{E_e E_\nu} + b\frac{m_e}{E_e} + \boldsymbol{\sigma}_n \cdot \left[A\frac{\mathbf{p}_e}{E_e} + B\frac{\mathbf{p}_\nu}{E_\nu}\right]\right), \quad (1)$$

where $\boldsymbol{\sigma}_n$ is the neutron spin, p_e is the momentum of the electron and p_ν is the momentum of the neutrino with energies E_e and E_ν, respectively, and E_0 is the endpoint energy of the electron. In the SM, $\xi = G_F^2 V_{ud}^2 (1 + 3\lambda^2)$, where $\lambda = g_A/g_V$ is the ratio of the axial-vector and vector coupling constants and G_F is the Fermi constant. The neutron decay observables include, a, the neutrino-electron correlation coefficient, b, the Fierz interference term, A, the beta asymmetry, and B, the neutrino asymmetry. Within the SM, the correlation coefficients a, A and B depend solely on the ratio of the axial-vector and vector coupling constants, $\lambda = g_A/g_V$. However the parameter, b, is included to account for the case of the hypothetical scalar or tensor couplings in addition to the (V-A) interaction of the SM. Many experiments are underway worldwide with the aim to improve the precision of measurements of these neutron decay observables, two importantly being the neutrino asymmetry B [3], and the Fierz interference term b [4,5]. The parameter b has linear sensitivity to BSM physics through [6]

$$b^{\mathrm{BSM}} = \frac{2}{1+3\lambda^2}[g_S \epsilon_S - 12\lambda g_T \epsilon_T] \approx 0.34 g_S \epsilon_S - 5.22 g_T \epsilon_T, \quad (2)$$

$$b_v^{\mathrm{BSM}} = \frac{2}{1+3\lambda^2}[g_S \epsilon_S \lambda - 4\lambda g_T \epsilon_T (1+2\lambda)] \approx 0.44 g_S \epsilon_S - 4.85 g_T \epsilon_T, \quad (3)$$

where ϵ_T and ϵ_S are the new-physics effective couplings and g_T and g_S are the tensor and scalar nucleon isovector charges. Here b_v^{BSM} is a correction term to the neutrino asymmetry correlation coefficient, B, and b^{BSM} is an addition to the Fierz interference term b in Eq. (1). Data taken at the Large Hadron Collider (LHC) is currently looking at probing scalar and tensor interactions at the $\lesssim 10^{-3}$ level [7]. However to fully assess the discovery potential of experiments at the 10^{-3} level it is crucial to identify existing constraints on new scalar and tensor operators.

Another quantity of interest is the neutron electric dipole moment (EDM), which is a measure for CP violation. In extensions of the Standard Model quarks acquire an EDM through the interaction of the photon with the tensor current [8]. The contribution of the quark EDMs, d_q, to the EDM of the neutron, d_n, is related to the quark tensor charges, g_T^q, by [9–11]

$$d_n = d_u g_T^d + d_d g_T^u + d_s g_T^s. \quad (4)$$

Here d_u, d_d, d_s, are the new effective couplings which contain new CP-violating interactions at the TeV scale. The current experimental data gives an upper limit on the neutron EDM of $|d_n| < 1.8 \times 10^{-26} e\,\mathrm{cm}$ [12]. In calculating the tensor charges and knowing a bound on d_n, we are able to constrain the couplings, d_q, and hence BSM theories.

In recent years there has been an increase in interest from lattice QCD Collaborations in calculating the axial, scalar and tensor isovector charges due to their importance in interpreting the results of many experiments and phenomena mediated by weak interactions [13–19]. The QCDSF/UKQCD/CSSM Collaborations have an ongoing program investigating various hadronic properties using the Feynman-Hellmann theorem [20–27]. Here we extend this work to a dedicated study of the nucleon tensor, scalar and axial charges. We discuss a flavor symmetry-breaking method to systematically approach the physical quark mass. We then extend this existing flavor-breaking expansion to also account for lattice spacing and finite volume effects to quantify systemic uncertainties. Finally, we look at the potential impact of our results on measurements of the Fierz interference term and the neutron EDM.

II. SIMULATION DETAILS

For this work we use gauge field configurations that have been generated with $N_f = 2 + 1$ flavors of dynamical fermions, using the tree-level Symanzik improved gluon action and nonperturbatively $\mathcal{O}(a)$ improved Wilson fermions [28]. In our simulations, we have kept the bare average quark mass, $\bar{m} = (m_u + m_d + m_s)/3$, held fixed approximately at its physical value, while systematically varying the quark masses around the $SU(3)$ flavor symmetric point, $m_u = m_d = m_s$, to extrapolate results to the physical point [29]. We also have degenerate u and d quark masses, $m_u = m_d \equiv m_l$. The coverage of lattice spacings and pion masses is represented graphically in Fig. 1.

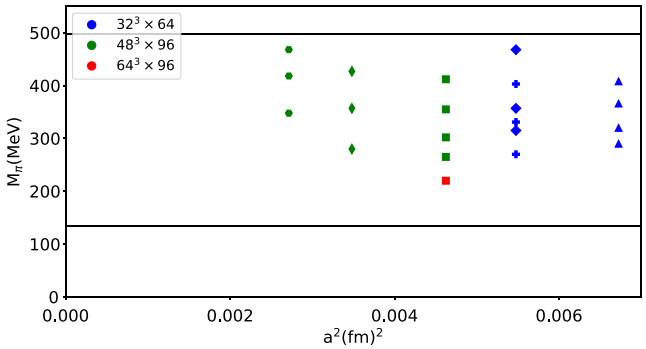

FIG. 1. Lattice ensembles that are used in this work characterized by pion mass, m_π, and lattice spacing, a. The horizontal lines represent the physical pion and kaon masses and the continuum limit occurs as $a \to 0$.

TABLE I. Details of lattice ensembles used in this work.

β	a (fm)	Volume	$(\kappa_{\text{light}}, \kappa_{\text{strange}})$	m_π	m_K (MeV)
5.40	0.082	$32^3 \times 64$	(0.119930, 0.119930)	408	408
			(0.119989, 0.119812)	366	424
			(0.120048, 0.119695)	320	440
			(0.120084, 0.119623)	290	450
5.50	0.074	$32^3 \times 64$	(0.120900, 0.120900)	468	468[a]
			(0.121040, 0.120620)	357	505[a]
			(0.121095, 0.120512)	315	526[a]
5.50	0.074	$32^3 \times 64$	(0.120950, 0.120950)	403	403
			(0.121040, 0.120770)	331	435
			(0.121099, 0.120653)	270	454
5.65	0.068	$48^3 \times 96$	(0.122005, 0.122005)	412	412
			(0.122078, 0.121859)	355	441
			(0.122130, 0.121756)	302	457
			(0.122167, 0.121682)	265	474
		$64^3 \times 96$	(0.122197, 0.121623)	220	485
5.80	0.059	$48^3 \times 96$	(0.122810, 0.122810)	427	427
			(0.122880, 0.122670)	357	456
			(0.122940, 0.122551)	280	477
5.95	0.052	$48^3 \times 96$	(0.123411, 0.123558)	468	395
			(0.123460, 0.123460)	418	418
			(0.123523, 0.123334)	347	451

[a]Ensembles with a different value of $\bar{m}$, further from the physical $\bar{m}$. The uncertainty on the pseudoscalar masses is between 1–3 MeV.

Further information about these ensembles is presented in Table I and Appendix A, Table VII. We have five lattice spacings, $a = 0.082$, 0.074, 0.068, 0.059, 0.052 fm [30], enabling an extrapolation to the continuum limit as well as three lattice volumes, $32^3 \times 64$, $48^3 \times 96$ and $64^3 \times 96$, allowing an extension to the flavor-breaking expansion, which describes the quark mass dependence of the matrix elements, to also account for lattice spacing and finite volume effects. We also use a bootstrapping resampling technique to compute all statistical uncertainties in our study.

In order to compare with existing results in the literature we use the renormalization constants given in Table II. Table II summarizes the renormalization constants at each value of β after chiral and continuum extrapolation across multiple masses with conversion from RI′-MOM to $\overline{\text{MS}}$ at $\mu = 2$ GeV. The renormalization constants are calculated following the method in Ref. [31] and the results first appeared in Ref. [32].

TABLE II. Renormalization constants at each value of β after chiral and continuum extrapolation across multiple masses with conversion from RI′-MOM to $\overline{\text{MS}}$ at $\mu = 2$ GeV [31,32].

β	$Z_T^{\overline{\text{MS}}}$	$Z_S^{\overline{\text{MS}}}$	Z_A
5.40	0.9637(23)	0.7034(48)	0.8671(77)
5.50	0.9644(49)	0.7046(89)	0.8693(38)
5.65	0.9684(54)	0.7153(86)	0.8754(19)
5.80	0.9945(11)	0.6709(23)	0.8913(49)
5.95	0.9980(42)	0.6683(94)	0.8983(43)

III. THE FEYNMAN-HELLMANN THEOREM

The Feynman-Hellmann (FH) theorem is used to calculate hadronic matrix elements in lattice QCD through modifications to the QCD Lagrangian. The expression for the FH theorem in the context of field theory is [20]

$$\frac{\partial E_{H,\lambda}(\vec{p})}{\partial \lambda} = \frac{1}{2E_{H,\lambda}(\vec{p})} \left\langle H, \vec{p} \left| \frac{\partial S}{\partial \lambda} \right| H, \vec{p} \right\rangle_\lambda, \tag{5}$$

where S is a modified action of our theory so that it depends on some parameter λ, $S \to S(\lambda)$ and $E_{H,\lambda}(\vec{p})$ is the energy of a hadron state, H. This result relates the derivative of the total energy to the expectation value of the derivative of the action with respect to the same parameter.

A. Application and implementation

Consider the following modification to the action of our theory,

$$S \to S + \lambda \mathcal{O}. \tag{6}$$

Then the FH theorem as shown in Eq. (5), provides a relationship between an energy shift and a matrix element of interest,

$$\left.\frac{\partial E_{H,\lambda}(\vec{p})}{\partial \lambda}\right|_{\lambda=0} = \frac{1}{2E_H(\vec{p})} \langle H, \vec{p} | \mathcal{O} | H, \vec{p} \rangle. \tag{7}$$

Importantly, the right-hand side is the standard matrix element of the operator $\mathcal{O}$ inserted on the hadron, H, in the absence of any background field. In lattice calculations, we modify the action in Eq. (6), then examine the behavior of hadron energies as the parameter λ changes, and finally extract the above matrix element from the slope at $\lambda = 0$.

In order to calculate the tensor, axial and scalar charges of a baryon, the extra terms we add to the QCD action are

$$S_T \to S + \zeta_{\mu\nu}^T \lambda \sum_x \bar{q}(x) \sigma_{\mu\nu} \gamma_5 q(x), \tag{8}$$

$$S_A \to S + \zeta_\mu^A \lambda \sum_x \bar{q}(x) \gamma_\mu \gamma_5 q(x), \tag{9}$$

$$S_S \to S + \lambda \sum_x \bar{q}(x) q(x), \tag{10}$$

where we will take the case of each quark flavor, q, separately, $\zeta_{\mu\nu}^T$, ζ_μ^A are the phase factors and there are four choices of μ and ν. The phase factors chosen here are $\zeta_{k4}^T = \zeta_{4j}^T = 1$, $\zeta_{kj}^T = i$ and $\zeta_4^A = 1$, $\zeta_k^A = i$. The tensor, axial and scalar charges are related to the baryon matrix elements of the same operators:

$$\langle \vec{p},\vec{s}|\mathcal{T}_{\mu\nu}|\vec{p},\vec{s}\rangle = -i\frac{2}{m}(s_\mu p_\nu - s_\nu p_\mu)g_T^q,$$
$$\langle \vec{p},\vec{s}|\mathcal{A}_\mu|\vec{p},\vec{s}\rangle = 2is_\mu g_A^q,$$
$$\langle \vec{p},\vec{s}|\mathcal{S}|\vec{p},\vec{s}\rangle = 2mg_S^q, \tag{11}$$

where $\mathcal{T}_{\mu\nu} = \bar{q}\sigma_{\mu\nu}\gamma_5 q$, $\mathcal{A}_\mu = \bar{q}\gamma_\mu\gamma_5 q$ and $\mathcal{S} = \bar{q}q$ [33]. In our simulations, we have chosen $\mu = 3$, $\nu = 4$ and $\vec{p} = 0$,

$$\langle \vec{0},\vec{s}|\mathcal{T}_{34}|\vec{0},\vec{s}\rangle = 2mg_T^q\sigma,$$
$$\langle \vec{0},\vec{s}|\mathcal{A}_3|\vec{0},\vec{s}\rangle = 2img_A^q\sigma,$$
$$\langle \vec{0},\vec{s}|\mathcal{S}|\vec{0},\vec{s}\rangle = 2mg_S^q, \tag{12}$$

where, $\sigma = \pm 1$, is the spin of the baryon polarized in the z direction.[1] Hence the FH theorem in Eq. (7) for the tensor and axial charges gives

$$\left.\frac{\partial E_\lambda^+}{\partial\lambda}\right|_{\lambda=0} = g_{T,A}^q, \qquad \left.\frac{\partial E_\lambda^-}{\partial\lambda}\right|_{\lambda=0} = -g_{T,A}^q, \tag{13}$$

where we have dropped the, H, subscript as from now on we are only dealing with baryon states and $E^{+/-}$ denotes the baryon energy with spin up/down in the z direction in the presence of a tensor or axial background field [Eqs. (8) and (9)] with strength λ. For small values of λ, the energy is therefore given by

$$E_\lambda^\pm = E_0 \pm \lambda g_{T,A}^q + \mathcal{O}(\lambda^3). \tag{14}$$

We have related the change in energy of the hadron state to the spin contribution from the quark flavor q. Alternatively, due to the combination of $\pm\lambda$, the spin-down state with positive λ is equivalent to the energy shift of the spin-up state with negative λ. For the scalar we simply have

$$\left.\frac{\partial E_\lambda}{\partial\lambda}\right|_{\lambda=0} = g_S^q,$$
$$E_\lambda = E_0 + \lambda g_S^q + \mathcal{O}(\lambda^2). \tag{15}$$

Here the insertion is on the quark flavor q. For example, we use the perturbed propagator for the d-quark in the proton to get the d-quark contribution to the nucleon isovector charge. The nucleon isovector charges are then given by the difference between the up- and down-quark contributions,

$$g_{T,A,S}^{u-d} = g_{T,A,S}^u - g_{T,A,S}^d. \tag{16}$$

Here we only insert the operator into the propagators used in the quark-line connected contributions; there are no quark-line disconnected terms considered here as they cancel in the case $u-d$. To improve the precision of our results we can take advantage of the fact that we are only interested in energy changes due to changes in λ, specifically the change in energy around the point $\lambda = 0$, with respect to the unperturbed energy. We consider two correlation functions, one calculated at $\lambda = 0$ and the other at some finite value of λ. If we take the ratio of these two quantities, we find

$$\frac{C_\lambda(t)}{C(t)} \overset{\text{large t}}{=} e^{-(E_\lambda - E)t}\frac{E}{E_\lambda}\frac{|A_\lambda|^2}{|A|^2}. \tag{17}$$

The exponential dependence on t now contains the difference in energies between the unperturbed energy and the energy at some λ. C and C_λ are both measured on the same configurations, so both will have correlated noise. Using this ratio to determine energy differences has the advantage that the noise will largely cancel, leaving to a more reliable energy shift. We can also constrain our fit function to pass through zero by construction as there is no difference in energies at $\lambda = 0$.

The extraction of hadron matrix elements in lattice QCD demands careful attention to contamination from excited states. Excited-state contamination has an impact on the study of standard baryon three-point functions due to the presence of weak signal-to-noise behavior at large Euclidean times. Various techniques are used to address excited-state contamination, one of which is the variational method. The variational method has been widely successful in spectroscopy investigations [34–40], and has also found application in the analysis of hadronic matrix elements [41–46]. Another popular method is the "two-exponential fit" and "summation" methods seen in Refs. [45–51]. A summary of these methods as well as a comparison between them can be seen in Ref. [52]. Since in this investigation hadron energies are extracted from two-point functions, control of excited state contamination in the Feynman-Hellmann is simplified compared to standard three-point analyses. For example Fig. 2 shows

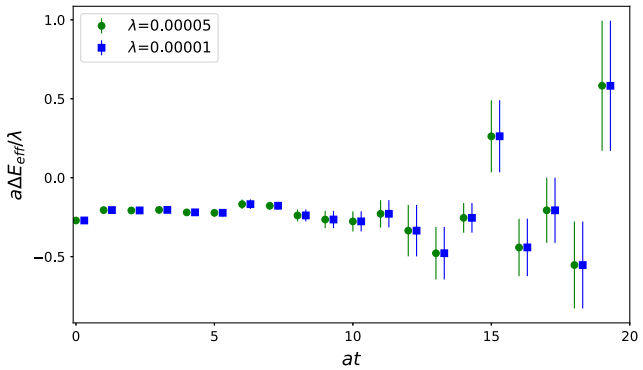

FIG. 2. Proton effective mass for the ratio [Eq. (17)] divided by λ, for the down quark at two different values of λ, calculated at $a = 0.068$ fm, $(\kappa_l, \kappa_s) = (0.122167, 0.121682)$ for the tensor. The points have been offset slightly for clarity.

[1]Our spin vector is given by $s(\vec{p}) = (i\frac{\vec{s}\cdot\vec{p}}{E}, \vec{s}(p))$, where $\vec{s}(\vec{p}) = \vec{e} + \frac{\vec{p}\cdot\vec{e}}{m(E+m)}\vec{p}$, with quantization axis $\vec{n}$ where $\vec{e} = \sigma m\vec{n}$, $\sigma = \pm 1$ and $s^2 = -m^2$. For our case we have $\mu = 3$, $\nu = 4$, $\vec{p} = 0$ and $\vec{n} = \vec{e}_3$. Therefore, $s_3 = \sigma m\vec{e}_3$, $s_4 = 0$ and $p_4 = im$.

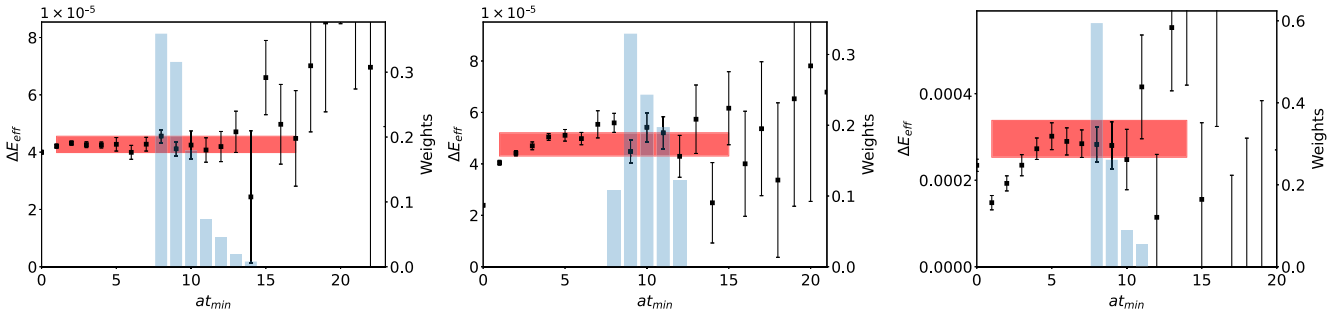

FIG. 3. Proton effective mass for the ratio [Eq. (17)] for the up quark at $\lambda = 0.00005$, for spin down in the tensor (a) and the axial (b) with the scalar results show in (c), calculated at $a = 0.068$ fm, $(\kappa_l, \kappa_s) = (0.122167, 0.121682)$. The blue bar graph shows the weight of each fit result for the value of t_{min}. The horizontal (red) band is the weighted-average value, where the band includes the combined statistical and systematic uncertainty.

the effective energy shift for the ratio [Eq. (17)] divided by λ for the down quark at two different values of λ. In Fig. 2 we see a plateau in the effective mass indicating a clear region where the ground state can be isolated.

IV. WEIGHTED-AVERAGING METHOD

The dependency of the fits on the time ranges used is a source of systematic uncertainty. To address these issues, we use a weighted-averaging method on the fit results to limit the impact of the fit window selection. The weighted averaging method we use is a simplified variation of that outlined in detail in Ref. [53] and has similarities to that proposed in Ref. [54]. We proceed by determining the energy shifts, $\Delta E = E_\lambda - E$, by fitting the ratio of perturbed to unperturbed correlation functions using Eq. (17) for a variety of different Euclidean time fit windows. The largest time slice employed in each fit for each ensemble and operator is fixed to be the last time slice before the signal is lost due to statistical noise. For example, in Fig. 2 this would be chosen to be $t_{\text{max}} \approx 17$. The start of the fit range, t_{min}, is varied between $t_{\text{min}/a} = 6, 7, 8, 9, 10$ for ensembles with $\beta = 5.40, 5.50, 5.65, 5.80, 5.95$, respectively and up to the largest value of t_{min} such that no less than four time slices are used in a fit. By adjusting the minimum time of the fit range, t_{min}, based on the lattice spacing of each ensemble, we are ensuring that each fit starts at an earlier scale. In the following we refer to the value of ΔE for a single fit, f, as E^f. Each fit result is then assigned a weight,

$$w^f = \frac{p_f (\delta E^f)^{-2}}{\sum_{f'=1}^{N} p_{f'} (\delta E^{f'})^{-2}}, \tag{18}$$

where f labels the choice of fit range specified by t_{min} for a fixed t_{max}, $p_f = \Gamma(N_{d.o.f.}/2, \chi^2/2)/\Gamma(N_{d.o.f.}/2)$ is the p-value of the fit and δE^f is the uncertainty in the energy shift, E^f, for fit f. Taking a weighted average of the N fit findings, E^f, provides the final estimate of the energy shift, $\bar{E}$, and associated uncertainty $\delta\bar{E}$,

$$\begin{aligned}
\bar{E} &= \sum_{f=1}^{N} w^f E^f, \\
\delta_{\text{stat}}\bar{E}^2 &= \sum_{f=1}^{N} w^f (\delta E^f)^2, \\
\delta_{\text{sys}}\bar{E}^2 &= \sum_{f=1}^{N} w^f (E^f - \bar{E})^2, \\
\delta\bar{E} &= \sqrt{\delta_{\text{stat}}\bar{E}^2 + \delta_{\text{sys}}\bar{E}^2}.
\end{aligned} \tag{19}$$

The total error $\delta\bar{E}$ describes the combined statistical uncertainty on $\bar{E}$ plus the systematic uncertainty arising from the choice of fit range. The separating of this error into $\delta_{\text{stat}}\bar{E}$ and $\delta_{\text{sys}}\bar{E}$ only partially separates statistical and systematic uncertainties because $\delta_{\text{stat}}\bar{E}$ includes statistical errors plus systematic uncertainties related to fluctuations among the δE^f. The final estimate, $\bar{E}$, provides an estimate of the energy of the hadron with reduced systematic bias arising from choice of fit window. Figure 3 shows the proton effective energy shift for the ratio [Eq. (17)], using the standard definition of an effective mass. The final estimate of the energy shift, $\bar{E}$, when using the weighted-averaging method is indicated by the red band. Figure 3 also includes a bar graph for the weights assigned to each fit value.

V. DETERMINATION OF MATRIX ELEMENTS

A. Feynman-Hellman method

Now that we have a procedure for reliably determining the energy shifts, we are now in a position to determine ΔE at multiple values of λ for a fixed ensemble and operator. In Fig. 4 we plot the calculated proton energy shifts ΔE for

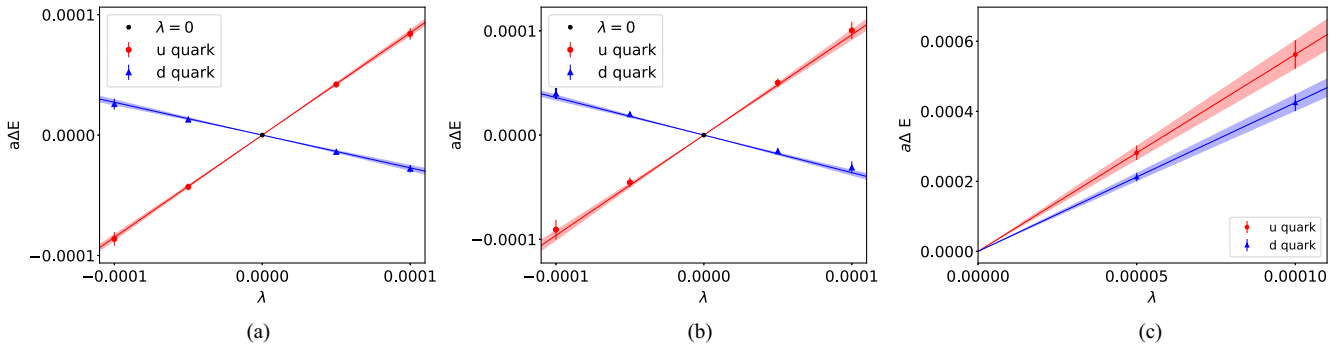

FIG. 4. Proton energy shift, $\Delta E = E_\lambda - E$, for different parameter values, with a linear fit, where the red and blue bands show the statistical errors associated with the fitted parameters. Calculated at $a = 0.068$ fm, $(\kappa_l, \kappa_s) = (0.122167, 0.121682)$. Results for the tensor (a), axial (b) and scalar (c) operators.

each value of λ for the $a = 0.068$ fm ensemble with $(\kappa_l, \kappa_s) = (0.122167, 0.121682)$. Figure 4(a) shows results for the tensor operator, while Fig. 4(b) shows those for the axial operator. Now performing a linear fit to Eq. (14) and extracting the slope we obtain the following results, $g_T^u = 0.822(27)$, $g_T^d = -0.263(25)$, $g_A^u = 0.814(56)$ and $g_A^d = -0.316(26)$, with the tensor results, renormalized at $\mu = 2$ GeV in the $\overline{\text{MS}}$ scheme using the renormalization factors given in Table II. Similarly for the scalar charge, in Fig. 4(c) we perform a linear fit to Eq. (15) and by extracting the slope we find, $g_S^u = 4.03(29)$ and $g_S^d = 3.04(17)$, again renormalized at $\mu = 2$ GeV in the $\overline{\text{MS}}$ scheme. The above process has been repeated for all quark masses on each of the lattice spacings as well as for the Σ and Ξ baryons. The results can been found in Appendix B, in Tables XIII, IX, and X.

B. Two-exponential fit method

Here we compare the FH method results to the popular "two-exponential fit" method using three point functions.

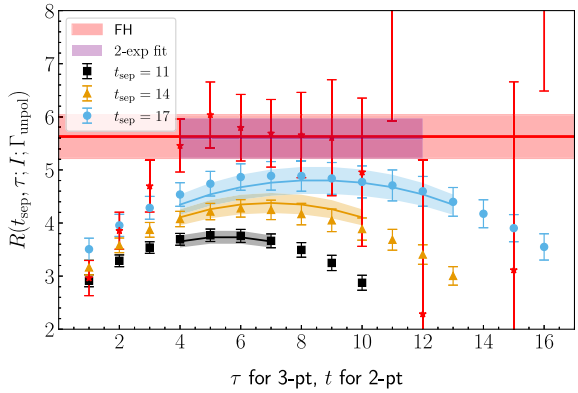

FIG. 5. Graph of g_S^u extracted using the FH method shown by the red points and shaded band compared with the result using the two-exponential fit method, calculated at $a = 0.068$ fm, $(\kappa_l, \kappa_s) = (0.122167, 0.121682)$. The black, orange and blue fits correspond to the two-exponential fit function constructed and the purple shaded area corresponds to the g_S^u parameter extracted from the two-exponential fit.

This is undertaken by expanding the two-point and three-point functions to the second energy state and fitting to obtain the parameters of interest. The process for the two-exponential fit is to fit the two-point correlator over a sink time range in which the two-state initial fit assumption is justified. Then using these extracted parameters in the fit to the three-point correlator using a τ range that also satisfies a two-state initial fit assumption. A detailed treatment of the two-exponential fit is given in, for example, Ref. [52]. Figure 5 shows a comparison of the result for g_S^u extracted using the FH method (red band) and the result using the two-exponential fit method (purple band). The red points come from a fixed λ value, similar to that shown in Fig. 2, whereas the red band comes from performing a linear fit to Eq. (14) and extracting the slope. We can see that the results using the FH method is in excellent agreement with the standard three-point analysis.

Now that we have the quark contributions for multiple lattice ensembles, in the next section we shall use a $SU(3)$ flavor symmetry breaking method to extrapolate results for the nucleon isovector charges to the physical quark mass.

VI. FLAVOR SYMMETRY BREAKING

The QCD interaction is flavor-blind, which means that the only distinction between quark flavors comes from the quark masses when we disregard the electromagnetic and weak interactions. The theory behind these interactions is easiest to understand when all three quark flavors share the same mass, as this allows us to use the full power of $SU(3)$ flavor symmetry. Here we have kept the bare quark mass, $\bar{m} = (m_u + m_d + m_s)/3$, held fixed at its physical value, while systematically varying the individual quark masses around the $SU(3)$ flavor symmetric point, $m_u = m_d = m_s$, in order to constrain the extrapolation to the physical point. In this work we simulate with degenerate u and d quark masses $m_u = m_d \equiv m_l$, restricting ourselves to $n_f = 2 + 1$.

When $SU(3)$ is unbroken all octet baryon matrix elements of a given octet operator can be expressed in terms of just two couplings f and d. However, once $SU(3)$ is broken and we move away from the symmetric point we can construct quantities (D_i, F_i) which are equal at the symmetric point but differ in the case where the quark masses are different. The theory behind constructing these quantities is described in detail in Ref. [55] and is summarized below. The result of constructing these quantities leads to "fan" plots, with slope parameters (r_i, s_i) relating them. Following the method in Ref. [55] we use the $SU(3)$ expansion to extrapolate the nucleon charges to the physical point.

In this work, we describe the quark mass dependence of the hadronic matrix elements by a perturbation in the quark masses about an $SU(3)$ symmetric point. This perturbation generates a polynomial expansion in the quark mass differences [i.e. the $SU(3)$ breaking parameter] and therefore appears distinct from a chiral formulation that generates nonanalytic behavior (e.g. logarithms) in the vicinity of the 2- or 3-flavor chiral limits. However, it has been demonstrated in Ref. [56], that by expanding the logarithmic features about a fixed quark mass point (such as the chosen $SU(3)$ symmetric point), the infrared singularities reveal themselves in the high-order terms of the polynomial expansion—hence demonstrating that the group-theoretic expansion does encode the same physics that appears in the logarithms. A detailed numerical investigation exploring the numerical convergence from both limits goes beyond the present work. Here we assess the convergence of our expansion empirically, subject to the precision of our numerical results.

A. Mass dependence of amplitudes

In order to find the allowed mass dependence of the octet operators in hadrons we need the $SU(3)$ decomposition of the $8 \otimes 8 \otimes 8$. $SU(3)$ singlet and octet coefficients are constructed through group theory and using a mass Taylor expansion, which can be seen in Ref. [55]. Here we summarize the coefficients in Table III.

These coefficients are used to construct equations which are linear in δm_l, where

$$\delta m_l = m_l - \bar{m}, \tag{20}$$

is the difference of the light quark mass to the $SU(3)$ symmetric point. Using the definitions in Table IV, we introduce the notation for the matrix element transition of $B \to B'$ as follows:

$$A_{\bar{B}'FB} = \langle B'|J^F|B\rangle, \tag{21}$$

where J^F is the appropriate operator, or current, from Table IV and F represents the flavor structure of the operator. From Table III we can now read off the expansions of the various matrix elements, where the f and d terms are independent of δm_l and the coefficients r_1, r_2, r_3 and s_1, s_2 are the leading order δm_l terms. For example if we look at the $\bar{\Sigma}\pi\Sigma$ term, we have to first order in δm_l,

$$\langle \Sigma^+|J^{\pi^0}|\Sigma^+\rangle = A_{\bar{\Sigma}\pi\Sigma} = 2f + (-2s_1 + \sqrt{3}s_2)\delta m_l. \tag{22}$$

TABLE III. Coefficients in the mass Taylor expansion of $A_{\bar{B}'FB}$ operator amplitudes: $SU(3)$ singlet and octet, for first-class currents [55].

		1, 1st class		8, 1st class				
		$\mathcal{O}(1)$		$\mathcal{O}(\delta m_l)$				
		f	d	d	d	d	f	f
I	$A_{\bar{B}'FB}$	f	d	r_1	r_2	r_3	s_1	s_2
0	$\bar{N}\eta N$	$\sqrt{3}$	-1	1	0	0	0	-1
0	$\bar{\Sigma}\eta\Sigma$	0	2	1	0	$2\sqrt{3}$	0	0
0	$\bar{\Lambda}\eta\Lambda$	0	-2	1	2	0	0	0
0	$\bar{\Xi}\eta\Xi$	$-\sqrt{3}$	-1	1	0	0	0	1
1	$\bar{N}\pi^0 N$	1	$\sqrt{3}$	0	0	-2	2	0
1	$\bar{\Sigma}\pi^0\Sigma$	2	0	0	0	0	-2	$\sqrt{3}$
1	$\bar{\Xi}\pi^0\Xi$	1	$-\sqrt{3}$	0	0	2	2	0

B. Mass dependence: Fan plots

Since we hold the average quark mass, $\bar{m}$, fixed, while moving away from the symmetric point, we only need to consider the nonsinglet polynomials in the quark mass. In this subsection quantities (D_i, F_i) are constructed which are equal at the symmetric point and differ in the case where the quark masses are different. We can then evaluate the violation of $SU(3)$ symmetry that emerges from the difference in $m_s - m_l$.

TABLE IV. The conventions for the generalized currents. We use the convention that current (i.e. operator) numbered by i has the same effect as absorbing a meson with the index i. Here γ represents an arbitrary Dirac matrix [55].

Index	Baryon (B)	Meson (F)	Current (J^F)
1	n	K^0	$\bar{d}\gamma s$
2	p	K^+	$\bar{u}\gamma s$
3	Σ^-	π^-	$\bar{d}\gamma u$
4	Σ^0	π^0	$\frac{1}{\sqrt{2}}(\bar{u}\gamma u - \bar{d}\gamma d)$
5	Λ^0	η	$\frac{1}{\sqrt{6}}(\bar{u}\gamma u + \bar{d}\gamma d - 2\bar{s}\gamma s)$
6	Σ^+	π^+	$\bar{u}\gamma d$
7	Ξ^-	K^-	$\bar{s}\gamma u$
8	Ξ^0	$\bar{K}^0$	$\bar{s}\gamma d$
0		η'	$\frac{1}{\sqrt{6}}(\bar{u}\gamma u + \bar{d}\gamma d + \bar{s}\gamma s)$

1. The d-fan

Following Ref. [55], we construct the following combinations of matrix elements which have the same value, $2d$, at the $SU(3)_d$ symmetric point:

$$\begin{aligned}
D_1 &\equiv -(A_{\bar{N}\eta N} + A_{\bar{\Xi}\eta\Xi}) = 2d - r_1\delta m_l,\\
D_2 &\equiv A_{\bar{\Sigma}\eta\Sigma} = 2d + (r_1 + 2\sqrt{3}r_3)\delta m_l,\\
D_3 &\equiv -A_{\bar{\Lambda}\eta\Lambda} = 2d - (r_1 + 2r_2)\delta m_l,\\
D_4 &\equiv \frac{1}{\sqrt{3}}(A_{\bar{N}\pi N} - A_{\bar{\Xi}\pi\Xi}) = 2d - \frac{4}{\sqrt{3}}r_3\delta m_l,\\
D_5 &\equiv A_{\bar{\Sigma}\pi\Lambda} = 2d + (r_2 - \sqrt{3}r_3)\delta m_l,\\
D_6 &\equiv \frac{1}{\sqrt{6}}(A_{\bar{N}K\Sigma} + A_{\bar{\Sigma}K\Xi}) = 2d + \frac{2}{\sqrt{3}}r_3\delta m_l,\\
D_7 &\equiv -(A_{\bar{N}K\Lambda} + A_{\bar{\Lambda}K\Xi}) = 2d - 2r_2\delta m_l.
\end{aligned} \tag{23}$$

By constructing these quantities the result is a "fan" plot with seven lines and three slope parameters (r_1, r_2 and r_3) constraining them. The slope parameters can be constrained by calculating octet baryon matrix elements on a set of ensembles with varying quark masses at fixed lattice spacing, such as those given in Table I, and constructing the D_is. For the forward matrix elements considered here, these D_is can also be written as linear combinations of the different quark contributions to the baryon charges. For example, using Table IV we see

$$\begin{aligned}
D_1 &= -(A_{\bar{N}\eta N} + A_{\bar{\Xi}\eta\Xi})\\
&= -\left(\frac{1}{\sqrt{6}}(g_p^u + g_p^d) + \frac{1}{\sqrt{6}}(g_\Xi^u - 2g_\Xi^s)\right),
\end{aligned} \tag{24}$$

where we introduce the notation g_B^q to denote the quark, q, contribution to the overall charge in the baryon, B. In this work we only consider the flavor diagonal matrix terms, i.e. there are no transition terms. Therefore, only the diagonal D terms, D_1, D_2 and D_4, are used. An "average D" can also be constructed from the diagonal amplitudes,

$$X_D = \frac{1}{6}(D_1 + 2D_2 + 3D_4) = 2d + \mathcal{O}(\delta m_l^2), \tag{25}$$

which is constant in δm_l up to terms $\mathcal{O}(\delta m_l^2)$. When constructing these fan plots it is useful to plot $\tilde{D}_i = D_i/X_D$ to find the average fit to reduce statistical fluctuations.

2. The f-fan

Similarly another five quantities, F_i, can be constructed which all have the same value, $2f$, at the $SU(3)_f$ symmetric point:

$$\begin{aligned}
F_1 &\equiv \frac{1}{\sqrt{3}}(A_{\bar{N}\eta N} - A_{\bar{\Xi}\eta\Xi}) = 2f - \frac{2}{\sqrt{3}}s_2\delta m_l,\\
F_2 &\equiv (A_{\bar{N}\pi N} + A_{\bar{\Xi}\pi\Xi}) = 2f + 4s_1\delta m_l,\\
F_3 &\equiv A_{\bar{\Sigma}\pi\Sigma} = 2f + (-2s_1 + \sqrt{3}s_2)\delta m_l,\\
F_4 &\equiv \frac{1}{\sqrt{2}}(A_{\bar{\Sigma}K\Xi} - A_{\bar{N}K\Sigma}) = 2f - 2s_1\delta m_l,\\
F_5 &\equiv \frac{1}{\sqrt{3}}(A_{\bar{\Lambda}K\Xi} - A_{\bar{N}K\Lambda}) = 2f + \frac{2}{\sqrt{3}}(\sqrt{3}s_1 - s_2)\delta m_l.
\end{aligned} \tag{26}$$

Again, an "average F" can be calculated through

$$X_F = \frac{1}{6}(3F_1 + F_2 + 2F_3) = 2f + \mathcal{O}(\delta m_l^2). \tag{27}$$

In this work, only the connected quark-line terms are computed. Quark-line disconnected terms only show up in the r_1 coefficient and r_1^{discon} cancels in the case $g_{T,A,S}^{u-d} = g_{T,A,S}^u - g_{T,A,S}^d$. Unlike the d-fan, the f-fan to linear order, has no error from dropping the quark-line disconnected contributions, as none of the r_i parameters appear in the f-fan.

C. Fan plot results

Here we present results using the $a = 0.068$ fm ensemble. Results from other lattice spacings are similar. In Sec. VII, we will extend this method to include all ensembles and present the final results for $g_{T,A,S}$. The singlet quantities X_D and X_F are calculated using Eqs. (25) and (27). In Fig. 6 X_D and X_F are plotted against δm_l and fitted to a constant. Since in Sec. VII we will work to $\mathcal{O}(\delta m_l^2)$ in our flavor-breaking expansions, we fit X_D and X_F to constants in order to determine their values at the physical quark masses. The constant fits to the $a = 0.068$ fm data are shown by the dashed lines in Fig. 6. In Fig. 7(a) we present the D-"fan" plot which shows the

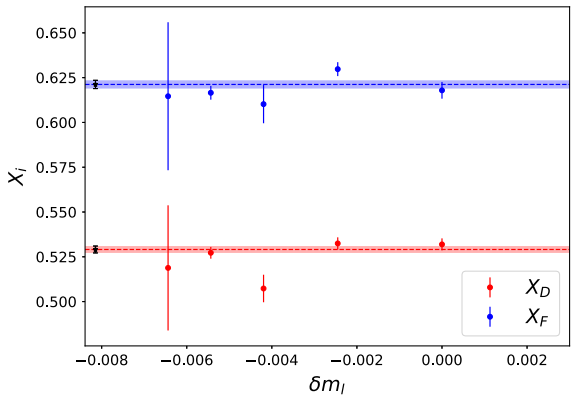

FIG. 6. X_D and X_F for each δm_l for the $a = 0.068$ fm ensemble for the tensor matrix element. The dashed lines are constant fits and the black stars represent the physical point.

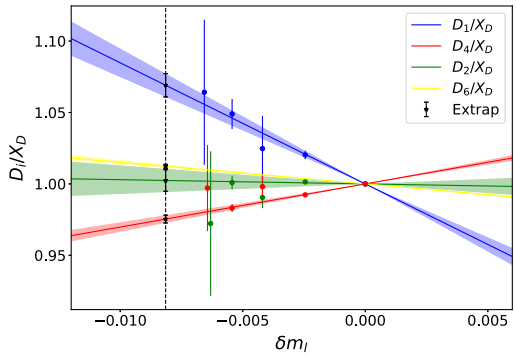

(a)

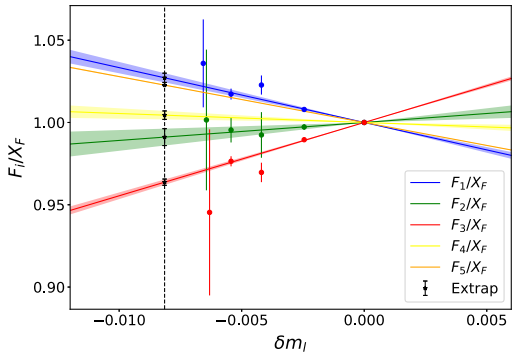

(b)

FIG. 7. (a) The three fits D_1, D_2 and D_4 (b) The three fits F_1, F_2 and F_3 for the tensor. The vertical black dotted line represents the physical point. Results for the five ensembles at $a = 0.068$ fm ensemble. The flavor off-diagonal terms D_6, F_4 and F_5 are also predicted and plotted. Where some points have been offset slightly for clarity.

δm_l dependence of the $\tilde{D}_i = D_i/X_D$ for $i = 1$, 2 and 4. Here the lines correspond to the linear in δm_l fits using Eq. (23). From these linear fits the slope parameters $\tilde{r}_1 = r_1/X_D$ and $\tilde{r}_3 = r_3/X_D$ are determined. It is interesting to note that these parameters also lead to a prediction for the flavor off-diagonal term for $i = 6$, which is also shown. Similarly in Fig. 7(b) we present the F-"fan" plot for $\tilde{F}_i = F_i/X_F$, $i = 1$, 2 and 3, where the lines correspond to the linear fits using Eq. (26). Similarly, the parameters $\tilde{s}_1 = s_1/X_F$ and $\tilde{s}_2 = s_2/X_F$ are determined from the linear fits. Again, the corresponding off-diagonal terms for $i = 4$, 5 are also predicted and plotted. By forming appropriate linear combinations, we reconstruct the matrix elements for an individual quark flavor in a particular hadron:

$$\langle p|\bar{u}\Gamma u|p\rangle = 2\sqrt{2}f + \left(\sqrt{\frac{3}{2}}r_1 - \sqrt{2}r_3 + \sqrt{2}s_1 - \sqrt{\frac{3}{2}}s_2\right)\delta m_l,$$

$$\langle p|\bar{d}\Gamma d|p\rangle = \sqrt{2}(f - \sqrt{3}d) + \left(\sqrt{\frac{3}{2}}r_1 + \sqrt{2}r_3 - \sqrt{2}s_1 - \sqrt{\frac{3}{2}}s_2\right)\delta m_l, \tag{28}$$

and hence the nucleon isovector charges can be determined,

$$g^{u-d}_{T,A,S} = \langle p|\bar{u}\Gamma u|p\rangle - \langle p|\bar{d}\Gamma d|p\rangle, \tag{29}$$

for $\Gamma = \sigma_{34}\gamma_5, \gamma_3\gamma_5$ and I. To obtain an extrapolation of $g_{T,A,S}$ to the physical point, we evaluate the expressions in Eq. (28) at $\delta m_l \to \delta m_l^*$ and substitute in the estimated values for $r_i = \tilde{r}_i X_D$ and $s_i = \tilde{s}_i X_F$. In order to quantify systemic uncertainties we will now extend this flavor breaking expansion method further.

VII. GLOBAL FITS

The flavour breaking expansion described in Sec. VI only accounts for the quark mass-dependence of the matrix elements. However, in order to quantify systematic uncertainties, here we extend this method to also account for lattice spacing, finite volume effects and second-order mass terms. As we are performing a global fit over all ensembles, we are now able to place constraints on the second-order mass terms, which means that all fits will now incorporate a term of order $\mathcal{O}(\delta m_l^2)$. These fits also include corrections with respect to a, a^2 and $m_\pi L$. In order to perform a global fit across all masses we substitute the quantity δm_l from here on with

$$\delta m_l \to \delta m_l = \frac{m_\pi^2 - X_\pi^2}{X_\pi^2}, \tag{30}$$

where the pseudoscalar mass-flavor singlet, X_π^2, is given by

$$X_\pi^2 = \frac{2m_K^2 + m_\pi^2}{3}. \tag{31}$$

By determining δm_l to now be dimensionless and given in terms of physical quantities we are now able to combine results from different lattice spacings. The fit used for the singlet quantities X_D and X_F are extended to [56],

$$X_{D,F} = X^*_{D,F}\left(1 + c_1\frac{1}{3}[f_L(m_\pi) + 2f_L(m_K)]\right) + c_2 a + c_3\delta m_l^2, \tag{32}$$

where we also consider an alternative $\mathcal{O}(a^2)$ lattice spacing dependence by replacing $c_2 a$ with $c_2 a^2$. The c_1 term estimates the finite-size effects, where the leading meson-loop contribution has the functional form [57],

$$f_L(m) = \left(\frac{m}{X_\pi}\right)^2 \frac{e^{-mL}}{\sqrt{mL}}. \tag{33}$$

It is important to note that here finite size effects are only included in the singlet quantities X_D and X_F and not in the D and F fan plot fits as the finite size corrections to the flavor-breaking coefficients determined by fits to, e.g. $\tilde{D}_i = D_i/X_D$ are expected to be subdominant compared to those in the corresponding singlet quantities. The fits used for the D fan, $\tilde{D}_i = D_i/X_D$, are of the form:

TABLE V. Table of results for each fit and the corresponding $\chi^2/d.o.f.$, renormalized, where appropriate, at $\mu = 2$ GeV in the $\overline{\text{MS}}$ scheme. The notation in the first column shows which corrections are included in Eqs. (32), (34), and (35). For example Fit 4 includes all corrections a, δm_l^2 and $m_\pi L$, while Fit 1 only includes an added δm_l^2 term, i.e. $c_1 = c_2 = b_i = e_i = 0$.

Fit		X_D	$\chi^2/d.o.f.$	X_F	$\chi^2/d.o.f.$	g_T	$\chi^2/d.o.f.$ D-Fan	$\chi^2/d.o.f.$ F-Fan
1.	δm_l^2	0.515(43)	1.88	0.6002(57)	1.74	1.035(13)	1.27	1.84
2.	$a, \delta m_l^2$	0.5251(81)	1.87	0.610(10)	1.74	1.000(27)	0.76	1.24
3.	$a^2, \delta m_l^2$	0.5211(59)	1.86	0.608(69)	1.74	1.016(18)	0.72	1.22
4.	$a, \delta m_l^2, m_\pi L$	0.5252(80)	1.98	0.611(10)	1.84	1.001(27)	1.35	1.97
5.	$a^2, \delta m_l^2, m_\pi L$	0.5212(59)	1.97	0.606(75)	1.84	1.017(18)	0.74	1.18
6.	$\delta m_l^2, m_\pi L$	0.516(43)	1.98	0.6005(50)	1.83	1.034(13)	0.78	1.21

Fit		X_D	$\chi^2/d.o.f.$	X_F	$\chi^2/d.o.f.$	g_A	$\chi^2/d.o.f.$ D-Fan	$\chi^2/d.o.f.$ F-Fan
1.	δm_l^2	0.583(21)	0.99	0.648(22)	0.81	1.262(60)	1.00	1.74
2.	$a, \delta m_l^2$	0.565(36)	1.02	0.656(39)	0.85	1.21(15)	1.03	1.80
3.	$a^2, \delta m_l^2$	0.572(26)	1.02	0.651(28)	0.85	1.231(95)	1.02	1.80
4.	$a, \delta m_l^2, m_\pi L$	0.563(36)	1.08	0.654(39)	0.90	1.21(15)	0.93	1.64
5.	$a^2, \delta m_l^2, m_\pi L$	0.574(27)	1.08	0.653(30)	0.90	1.231(95)	0.95	1.73
6.	$\delta m_l^2, m_\pi L$	0.584(22)	1.04	0.648(22)	0.85	1.262(60)	0.95	1.73

Fit		X_D	$\chi^2/d.o.f.$	X_F	$\chi^2/d.o.f.$	g_S	$\chi^2/d.o.f.$ D-Fan	$\chi^2/d.o.f.$ F-Fan
1.	δm_l^2	−0.610(53)	1.03	2.52(12)	1.52	1.07(20)	1.29	2.76
2.	$a, \delta m_l^2$	−0.72(10)	0.98	2.58(15)	1.57	1.12(50)	1.30	2.87
3.	$a^2, \delta m_l^2$	−0.654(67)	0.99	2.55(13)	1.57	1.09(31)	1.30	2.89
4.	$a, \delta m_l^2, m_\pi L$	−0.71(10)	1.04	2.59(17)	1.67	1.11(50)	1.07	2.85
5.	$a^2, \delta m_l^2, m_\pi L$	−0.655(66)	1.05	2.52(14)	1.66	1.10(31)	1.07	2.99
6.	$\delta m_l^2, m_\pi L$	−0.608(54)	1.09	2.51(12)	1.60	1.06(19)	1.07	2.98

$$\tilde{D}_1 = 1 - 2(\tilde{r}_1 + \tilde{b}_1 a)\delta m_l + \tilde{d}_1 \delta m_l^2,$$
$$\tilde{D}_2 = 1 + ((\tilde{r}_1 + \tilde{b}_1 a) + 2\sqrt{3}(\tilde{r}_3 + \tilde{b}_3 a))\delta m_l + \tilde{d}_2 \delta m_l^2,$$
$$\tilde{D}_4 = 1 - \frac{4}{\sqrt{3}}(\tilde{r}_3 + \tilde{b}_3 a)\delta m_l + \tilde{d}_4 \delta m_l^2, \tag{34}$$

and similarly for the F fan, $\tilde{F}_i = F_i/X_F$:

$$\tilde{F}_1 = 1 - \frac{2}{\sqrt{3}}(\tilde{s}_2 + \tilde{e}_2 a)\delta m_l + \tilde{f}_1 \delta m_l^2,$$
$$\tilde{F}_2 = 1 + 4(\tilde{s}_1 + \tilde{e}_1 a)\delta m_l + \tilde{f}_2 \delta m_l^2$$
$$\tilde{F}_3 = 1 + (-2(\tilde{s}_1 + \tilde{e}_1 a) + \sqrt{3}(\tilde{s}_2 + \tilde{e}_2 a))\delta m_l + \tilde{f}_3 \delta m_l^2. \tag{35}$$

The δm_l^2 coefficients were computed for the EM form factors in Ref. [55]. At $\mathcal{O}(\delta m_l^2)$ there are 12 amplitudes and 11 coefficients so there is just one constraint. However, here we only consider the diagonal amplitudes and therefore we do not have 12 amplitudes and hence they are unable to be constrained here [58]. Therefore, they are replaced with one δm_l^2 coefficient $(\tilde{d}_i, \tilde{f}_i)$ for each D_i and F_i.

Now we perform a combination of different fits summarized in Table V. Firstly, the fit is performed individually on X_D and X_F. An example of this is shown in Figs. 8(a) and 8(c). In Fig. 8(a) we show X_F as a function $\frac{m_\pi^2 - X_\pi^2}{X_\pi^2}$ for "Fit 1," which only includes the constant term, X_F^* and a δm_l^2 term in Eq. (32), while Fig. 8(c) shows X_F as a function of $\frac{m_\pi^2 - X_\pi^2}{X_\pi^2}$ with the result from using Eq. (32) with all corrections included (Fit 4). The extrapolated result for X_D and X_F are summarized in Table V taken in the limits $a \to 0$, $m_\pi L \to \infty$ and $m_\pi, m_K \to$ physical masses. Similarly, fits are performed on the fan plots using Eqs. (34) and (35). Figures 8(b) and 8(d) show the results when using "Fit 1" and "Fit 4," where it is important to mention that all data points are shifted in the limit $a \to 0$ in Figs. 8(c) and 8(d). The slope results are then multiplied by the extrapolated results for X_D and X_F:

$$r_i = (\tilde{r}_i + \tilde{b}_i a)X_D,$$
$$s_i = (\tilde{s}_i + \tilde{e}_i a)X_F,$$
$$d_i = \tilde{d}_i X_D,$$
$$f_i = \tilde{f}_i X_F. \tag{36}$$

The resulting slope parameters r_i, s_i and the δm_l^2 coefficients are then included in the reconstruction of the matrix elements in a particular hadron,

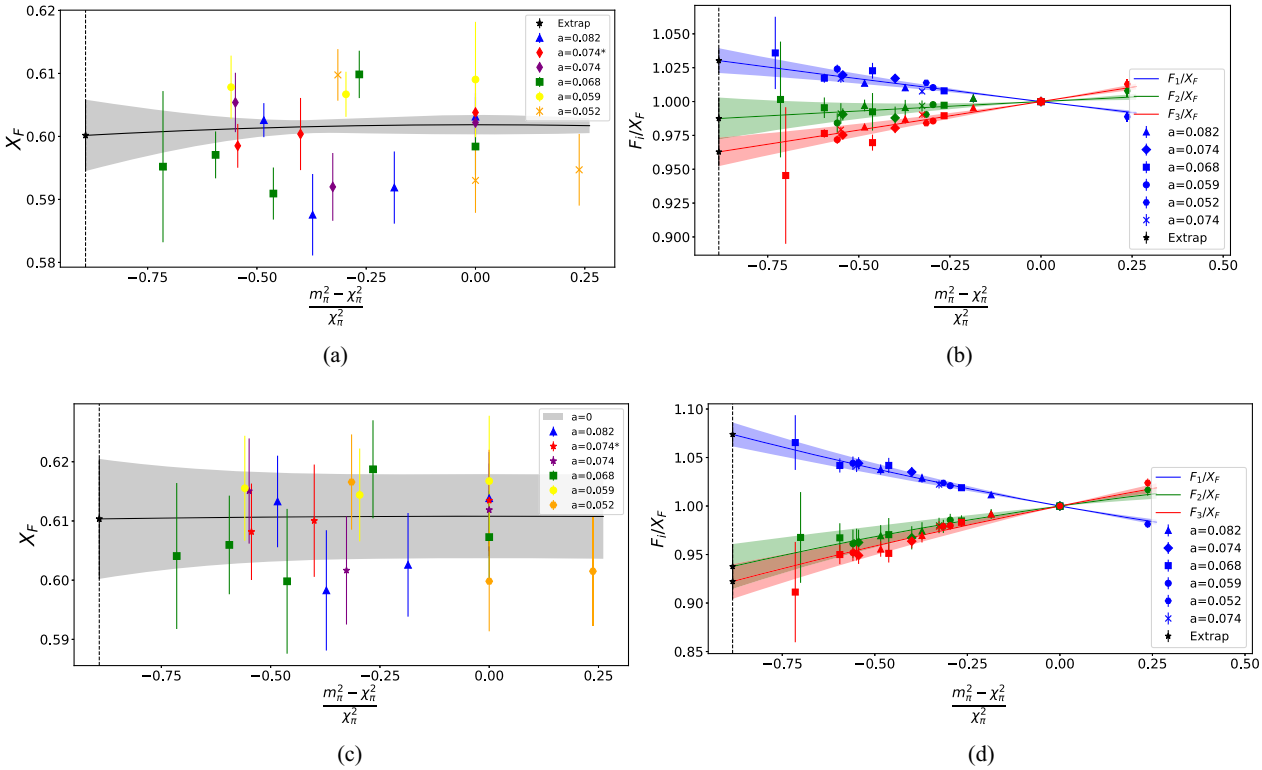

FIG. 8. As an example of some fits we have for the tensor: (a) X_F results for each ensemble using Eq. (32) where $c_1 = c_2 = 0$ (Fit 1), plotted against $\frac{m_\pi^2 - X_\pi^2}{X_\pi^2}$. (b) The three fits F_1, F_2 and F_3 using Eq. (35) with $e_i = 0$ (Fit 1). (c) X_F results using all corrections in Eq. (32) (Fit 4), plotted against $\frac{m_\pi^2 - X_\pi^2}{X_\pi^2}$. The black line is a fit to Eq. (32) in the limit $a \to 0$ and $m_\pi L \to \infty$. (d) The three fits F_1, F_2 and F_3 using Eq. (35), where once again the data points are shifted in the limit $a \to 0$. The black stars represent the physical point. Where some points have been offset slightly for clarity.

$$\begin{aligned}\langle p|\bar{u}\Gamma u|p\rangle &= 2\sqrt{2}f + \left(\sqrt{\frac{3}{2}}r_1 - \sqrt{2}r_3 + \sqrt{2}s_1 \right.\\ &\quad \left. - \sqrt{\frac{3}{2}}s_2\right)\delta m_l^* + \left(-\frac{\sqrt{3}}{2\sqrt{2}}d_1 + \frac{\sqrt{3}}{2\sqrt{2}}d_4 \right.\\ &\quad \left. + \frac{3}{2\sqrt{2}}f_1 + \frac{1}{2\sqrt{2}}f_2\right)\delta m_l^{*2},\\ \langle p|\bar{d}\Gamma d|p\rangle &= \sqrt{2}(f - \sqrt{3}d) + \left(\sqrt{\frac{3}{2}}r_1 + \sqrt{2}r_3 - \sqrt{2}s_1 \right.\\ &\quad \left. - \sqrt{\frac{3}{2}}s_2\right)\delta m_l^* + \left(-\frac{\sqrt{3}}{2\sqrt{2}}d_1 - \frac{\sqrt{3}}{2\sqrt{2}}d_4 \right.\\ &\quad \left. + \frac{3}{2\sqrt{2}}f_1 - \frac{1}{2\sqrt{2}}f_2\right)\delta m_l^{*2}, \end{aligned} \tag{37}$$

where $d = X_D^*/2$ and $f = X_F^*/2$. The final result for $g_{T,A,S}$ are then given in the limit, $a \to 0$, $m_\pi L \to \infty$ and δm_l^* is the physical mass. The final results for X_D, X_F and $g_{T,A,S}$ for each fit are summarized are in Table V, together with the χ^2_{reduced} for each fit.

A. Results

In order to combine these results we extend our weighted-averaging method described in Sec. IV. To do this we combine the χ^2 and degrees of freedom of X_D, X_F, D-fan and F-fan; enumerated by $i = 1, 2, 3, 4$, respectively, in the following:

$$\chi_f^2 = \sum_{i=1}^{4}\chi_i^2, \qquad N_{d.o.f.,f} = \sum_{i=1}^{4} N_{d.o.f.,i}, \tag{38}$$

where f labels one of the six fit types. Each fit is then assigned a weight using the combined χ_f^2,

$$\tilde{w}^f = \frac{p_f(\delta g^f_{T,A,S})^{-2}}{\sum_{f'=1}^{6} p_{f'}(\delta g^{f'}_{T,A,S})^{-2}}, \tag{39}$$

where $p_f = \Gamma(N_{d.o.f.,f}/2, \chi_f^2/2)/\Gamma(N_{d.o.f.,f}/2)$ is the p-value of the fit f and $\delta g^f_{T,A,S}$ is the uncertainty in the nucleon isovector charges calculated using Eq. (37). Taking a weighted average of the six fit results, $g^f_{T,A,S}$, provides a final estimate of the nucleon isovector charges, $g_{T,A,S}$, and associated uncertainty:

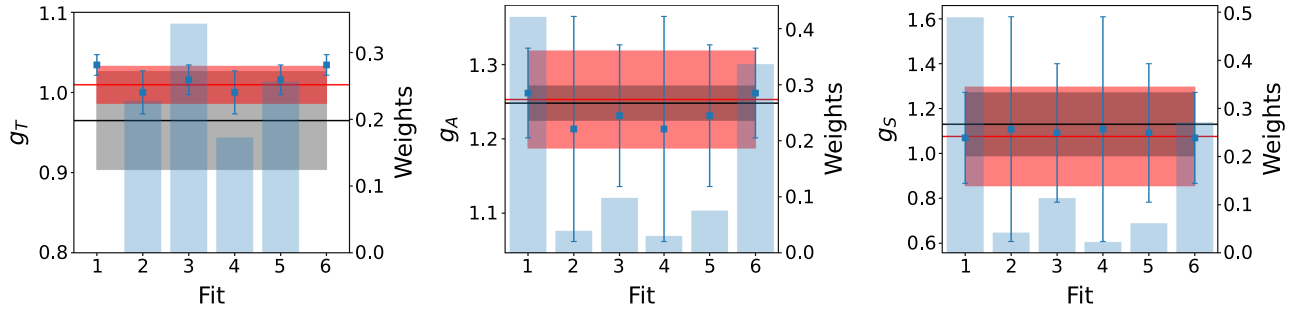

FIG. 9. Weighted average results for g_T, g_A and g_S. The x-axis displays the fit number as shown in Table V and the y-axis displays the corresponding nucleon isovector charge results. The bar graph shows the weight of each fit result. The red band shows the final weighted average result using Eq. (40), with statistical and systematic errors combined in quadrature and the gray band is the FLAG Review result [59].

$$\bar{g}_{T,A,S} = \sum_{f=1}^{6} w^f g^f_{T,A,S},$$
$$\delta_{\text{stat}}\bar{g}^2_{T,A,S} = \sum_{f=1}^{6} w^f (\delta g^f_{T,A,S})^2,$$
$$\delta_{\text{sys}}\bar{g}^2_{T,A,S} = \sum_{f=1}^{6} w^f (g^f_{T,A,S} - \bar{g}_{T,A,S})^2,$$
$$\delta\bar{g}_{T,A,S} = \sqrt{\delta_{\text{stat}}\bar{g}^2_{T,A,S} + \delta_{\text{sys}}\bar{g}^2_{T,A,S}}. \quad (40)$$

Figure 9 shows the results for each fit and their assigned weight. The final estimate of the nucleon isovector charges, $\bar{g}_{T,A,S}$, renormalized using the results given in Table II, at $\mu = 2$ GeV in the $\overline{\text{MS}}$, are

$$g_T = 1.010(21)_{\text{stat}}(12)_{\text{a}}(01)_{\text{FV}}, \quad (41)$$
$$g_A = 1.253(63)_{\text{stat}}(41)_{\text{a}}(03)_{\text{FV}}, \quad (42)$$
$$g_S = 1.08(21)_{\text{stat}}(03)_{\text{a}}(00)_{\text{FV}}, \quad (43)$$

where the systematic errors labeled as "a" and "FV" represent the difference in the central value obtained by incorporating a lattice spacing correction compared to without, and likewise for the finite-volume correction. These final results, with statistical and systematic errors combined in quadrature, are shown by the red bands in Fig. 9. We note our results for g_T, g_A and g_S are all comparable with the FLAG Review results [59], represented by the gray bands in Fig. 9. Of particular note is that we have determined g_T to the ≈2% level. However, work is still needed in order reduce the uncertainties on, g_S and g_A, to understand it at the same level.

As a check on our method for combining the results from the six different fits given in Table V, we employ the widely used Akaike information criterion (AIC). Here results obtained from the various fits are weighted using the Akaike weights [60],

$$w_f = \frac{\exp\left(-\frac{1}{2}\text{AIC}_f(\Gamma)\right)}{\sum_{f'}\exp\left(-\frac{1}{2}\text{AIC}_{f'}(\Gamma)\right)}. \quad (44)$$

Akaike's information criterion takes on the simple form for models with normally distributed errors:

$$\text{AIC}_f(\Gamma) = \chi^2_f + 2p_f, \quad (45)$$

where χ^2_f is the same as that calculated in Eq. (38) and p_f is the number of parameters in each fit. As a result the AIC weight prefers the models with lower χ^2 values, but penalizes those with too many fit parameters. The above method was repeated using the AIC weights. This gives the following results for the nucleon isovector charges, $g_T = 1.003(26)$, $g_A = 1.261(68)$ and $g_S = 1.07(23)$, where the errors have been added in quadrature. These results are in agreement with those in Eqs. (41)–(43).

B. Hyperons

Here we calculate flavor-diagonal matrix elements of hyperons using the same method. Reference [61] demonstrates that isovector combinations of hyperon charges are relevant in searches for new physics through semileptonic hyperon decays. The calculated slope parameters r_i, s_i and the δm_l^2 coefficients can also be used in the reconstruction of the matrix elements in a particular hyperon. The theory behind constructing these quantities

TABLE VI. Summary of results for the tensor, axial and scalar charges of the Σ^+ and Ξ^0 baryons. The first set of brackets contains the statistical uncertainty, whereas the second set of brackets contains the systematic uncertainty.

	Tensor	Axial	Scalar
$g^u_{\Sigma^+}$	0.802(16)(12)	0.884(25)(36)	2.75(25)(08)
$g^s_{\Sigma^+}$	−0.2379(10)(08)	−0.250(22)(30)	1.86(16)(12)
$g^u_{\Xi^0}$	−0.1929(77)(13)	−0.198(22)(15)	1.52(11)(08)
$g^s_{\Xi^0}$	0.968(25)(10)	0.924(23)(12)	2.58(24)(11)

is described in detail in Ref. [55] and is summarized in Appendix. C. The results for the charges of the Σ^+ and Ξ^0 baryons are summarized in Table VI.

To properly exploit the increased experimental sensitivity to hypothetical tensor and scalar interactions, we require lattice-QCD estimates of the nucleon isovector charge, g_T at the level of 10–20% [6]. The results presented here are at the $\delta g_T/g_T \approx 2\%$ level. As the overall goal of this research is to support precision tests of the Standard Model, we have successfully demonstrated the validity of our approach. We can now look at the effect this has on phenomenology.

VIII. IMPACT OF LATTICE RESULTS ON PHENOMENOLOGY

As discussed in Sec. I, it is expected that future neutron beta decay experiments will increase their sensitivity to BSM scalar and tensor interactions through improved measurements of the Fierz interference term, b, as well as the neutrino asymmetry parameter, B. In order to assess the full impact of these future experiments we have performed an analysis of the tensor charge g_T and g_S. Here we discuss existing constraints on new scalar ϵ_S and tensor ϵ_T couplings which arise from low-energy experiments. Finally, using the existing constraints on ϵ_S and ϵ_T as well as our calculated value for g_T and g_S, we determine the allowed regions in the $\epsilon_S - \epsilon_T$ plane.

A. Low-energy phenomenology of scalar and tensor interactions

1. $0^+ \to 0^+$ transitions and scalar interactions

The most precise bound on the scalar coupling ϵ_S comes from $0^+ \to 0^+$ nuclear beta decay. The differential decay rate for $0^+ \to 0^+$ nuclear beta decay has coefficient a_{0+} and Fierz interference term b_{0+} [6]:

$$a_{0+} = 1, \tag{46}$$

$$b_{0+} = -2\gamma g_S \epsilon_S, \qquad \gamma = \sqrt{1-\alpha^2 Z^2}, \tag{47}$$

where Z is the atomic number of the daughter nucleus. We can see from Eq. (47) that b_{0+} couples to the BSM scalar interaction. From a comparison of well-known half-lives corrected by a phase-space factor, Hardy and Towner [62] found $b_{0+} = -0.0022(26)$. This result was found using a number of daughter nuclei and averaging over the set. This can be converted to the following bound on the product of scalar charge and the new-physics effective scalar coupling,

$$-1.0 \times 10^{-3} < g_S \epsilon_S < 3.2 \times 10^{-3} \quad (90\%\ \text{CL}). \tag{48}$$

This is the most precise bound on the scalar interactions from low-energy probes.

2. Radioactive pion decay and the tensor interaction

An analysis of radioactive pion decay $\pi^+ \to e^+ \nu_e \gamma$ is sensitive to the same tensor operator that can be investigated in beta decays. The experimental results from the PIBETA Collaboration [63] put constraints on ϵ_T,

$$-1.1 \times 10^{-3} < \epsilon_T < 1.36 \times 10^{-3} \quad (90\%\ \text{CL}). \tag{49}$$

Currently this is the most stringent constraint on the tensor coupling from low-energy experiments. Using these constraints, as well Eqs. (2) and (3), bounds can be put on the new scalar and tensor interactions at the 10^{-3} level. Following the work of Ref. [6], in Fig. 10 we show the constraint on the ϵ_S-ϵ_T plane. The current best constraints on scalar and tensor interactions arise from $0^+ \to 0^+$ nuclear beta decays and radioactive pion decay, which is shown by the green band [6,62]. The neutron constraints are future projections at the 10^{-3} level, derived from Eqs. (2) and (3), using the tensor and scalar charges as obtained in this work, shown by the red and blue bands in Fig. 10. When accounting for uncertainties in these lattice QCD calculations, the boundaries on the bands in Fig. 10 become wider and the bands take on a "bow-tie" shape. However most of the constraining power is lost due to the large uncertainty in our value for g_S. In order to fully utilize the constraining power of 10^{-3} experiments, understanding the lattice-QCD estimates of the nucleon tensor and scalar charge at the level of 10% is required [6]. We have successfully calculated the tensor charge at the ≈2% level and are able to fully utilize the constraining power future experiments.

B. Quark electric-dipole moment

In this section we briefly discuss the impact our results have on constraining the quark EDM couplings using the current bound on the neutron EDM. Using the same method followed in Sec. VII we are able to constrain g_T^q. We note that in this work we have only considered quark-line connected contributions, although other works have shown the disconnected contributions to be small at near-physical quark masses [64]. This is in line with expectations based on the fact that the tensor operator is a helicity-flip operator and hence disconnected contributions mush vanish in the chiral limit.

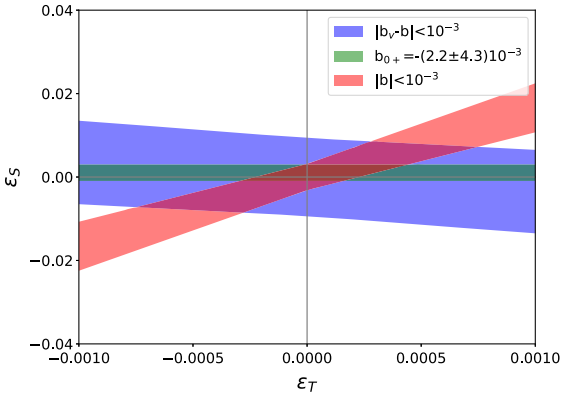

FIG. 10. Allowed regions in the $\epsilon_S - \epsilon_T$ plane, using the tensor and scalar charges as obtained in this work in Eqs. (41) and (43), $g_S = 1.08(21)_{\text{stat}}(03)_{\text{sys}}$ and $g_T = 1.010(21)_{\text{stat}}(12)_{\text{sys}}$. The green band is the existing band on b_{0+} [6,62].

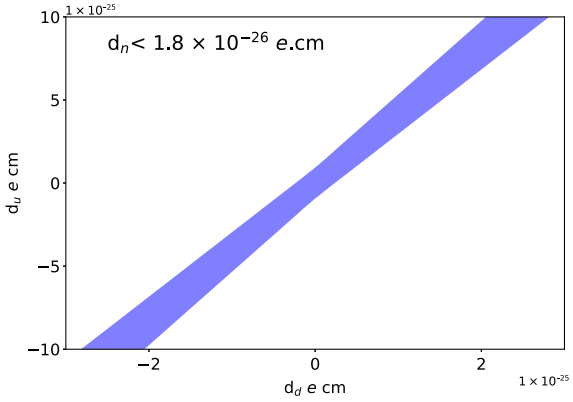

FIG. 11. 90% confidence level bounds on d_u and d_d using lattice QCD estimates for g_T^u and g_T^d and the current limit on the neutron EDM of $|d_n| < 1.8 \times 10^{-26} e\,\mathrm{cm}$ [12].

Using Eq. (37) we can calculate the up and down contributions to the nucleon tensor charge for each fit listed in Table V. Applying the weighted averaging method, the final estimates for, g_q^T, are

$$g_T^u = 0.812(21), \tag{50}$$

$$g_T^d = -0.199(14). \tag{51}$$

Using these results, Eq. (4) and the existing bound on the neutron EDM we are able to put bounds on the new effective couplings which contain new CP-violating interactions. Figure 11 shows the 90% confidence level bounds in the d_u-d_d plane, assuming $g_T^s = 0$.

IX. CONCLUSION

In this work we have presented results for the axial, tensor and scalar nucleon and hyperon charges using the Feynman-Hellmann theorem, as well as using a flavor symmetry breaking method to systematically approach the physical quark masses. We applied a weighted averaging method on the fit results, removing possible systematic uncertainties which arise from a bias in choosing the fit windows. In the flavor symmetry-breaking method, symmetry constraints are automatically built in order-by-order in $SU(3)$ breaking. We extended the flavor symmetry-breaking method in this analysis in order to have full coverage of a, m_π and volume, meaning we have control over these systematics. Our final result of $g_T = 1.010(21)_{\mathrm{stat}}(12)_{\mathrm{sys}}$ is comparable to results present in the FLAG review. We have precisely calculated g_T to the ≈2% level, successfully reaching the goal of understanding g_T at the 10% level. However, work is still needed in order reduce the error on, $g_S = 1.08(21)_{\mathrm{stat}}(03)_{\mathrm{sys}}$ and $g_A = 1.253(63)_{\mathrm{stat}}(41)_{\mathrm{sys}}$, to understand it at the same level. Future work is still needed with access to physical quark masses in order to better constrain the extrapolation to the physical point.

ACKNOWLEDGMENTS

The numerical configuration generation (using the BQCD lattice QCD program [65]) and data analysis (using the Chroma software library [66]) was carried out on the DiRAC Blue Gene Q and Extreme Scaling Service (EPCC, Edinburgh, UK), the Data Intensive Service (Cambridge Service for Data-Driven Discovery, CSD3, Cambridge, UK), the Gauss Centre for Supercomputing (GCS) supercomputers JUQUEEN and JUWELS (John von Neumann Institute for Computing, NIC, Jülich, Germany) and resources provided by the North-German Supercomputer Alliance (HLRN), the National Computer Infrastructure (NCI National Facility in Canberra, Australia supported by the Australian Commonwealth Government) and the Phoenix HPC service (University of Adelaide). R. H. is supported in part by the STFC Grant No. ST/P000630/1. P. E. L. R. is supported in part by the STFC Grant No. ST/G00062X/1. G. S. is supported by DFG Grant No. SCHI 179/8-1. R. D. Y. and J. M. Z. are supported by the ARC Grants No. DP190100298 and No. DP220103098.

APPENDIX A: LATTICE ENSEMBLE DETAILS

TABLE VII. Details of the lattice ensembles used in this work: the same number of configurations was used for each λ value and operator. Measurements are separated by a single HMC trajectory with a randomized source location. The number in parentheses indicates the quantity of randomized sources used per configuration to generate additional samples.

β	a (fm)	Volume	$(\kappa_{\mathrm{light}}, \kappa_{\mathrm{strange}})$	#Trajectories
5.40	0.082	$32^3 \times 64$	(0.119930, 0.119930)	1639
			(0.119989, 0.119812)	1005(2)
			(0.120048, 0.119695)	1000(3)
			(0.120084, 0.119623)	1345(3)
5.50	0.074	$32^3 \times 64$	(0.120900, 0.120900)	1754
			(0.121040, 0.120620)	1216
			(0.121095, 0.120512)	1849(2)
5.50	0.074	$32^3 \times 64$	(0.120950, 0.120950)	1614
			(0.121040, 0.120770)	1762
			(0.121099, 0.120653)	1003(2)
5.65	0.068	$48^3 \times 96$	(0.122005, 0.122005)	531
			(0.122078, 0.121859)	633
			(0.122130, 0.121756)	561(2)
			(0.122167, 0.121682)	534(2)
		$64^3 \times 96$	(0.122197, 0.121623)	428(3)
5.80	0.059	$48^3 \times 96$	(0.122810, 0.122810)	298
			(0.122880, 0.122670)	458(2)
			(0.122940, 0.122551)	522
5.95	0.052	$48^3 \times 96$	(0.123411, 0.123558)	283(2)
			(0.123460, 0.123460)	457
			(0.123523, 0.123334)	415

APPENDIX B: INDIVIDUAL QUARK CONTRIBUTIONS TO THE OVERALL CHARGE IN THE BARYON

Here we present the bare results for the individual quark contributions to the overall tensor, axial and scalar charges in the nucleon, Σ and Ξ baryons.

TABLE VIII. Table of the bare results for the individual quark contributions to the overall tensor charge in the nucleon, Σ and Ξ baryons.

β	κ_l	$g^u_{T_P}$	$g^d_{T_P}$	$g^u_{T_\Sigma}$	$g^s_{T_\Sigma}$	$g^u_{T_\Xi}$	$g^s_{T_\Xi}$
5.40	0.119930	0.8851(55)	−0.2020(43)	0.8851(55)	−0.2020(43)	−0.2020(43)	0.8851(55)
	0.119989	0.832(23)	−0.222(10)	0.838(25)	−0.216(18)	−0.222(18)	0.851(24)
	0.120048	0.849(24)	−0.225(17)	0.845(25)	−0.2145(83)	−0.209(11)	0.870(11)
	0.120084	0.842(32)	−0.209(25)	0.830(17)	−0.2098(61)	−0.2112(97)	0.8760(83)
5.50	0.120900	0.869(10)	−0.2145(34)	0.869(10)	−0.2145(34)	−0.2145(34)	0.869(10)
	0.121040	0.810(38)	−0.202(22)	0.809(25)	−0.2163(98)	−0.2042(83)	0.8796(85)
	0.121095	0.800(27)	−0.198(22)	0.822(17)	−0.2159(66)	−0.1947(59)	0.8747(61)
5.50	0.120950	0.8830(59)	−0.2115(39)	0.8830(59)	−0.2115(39)	−0.2115(39)	0.8830(59)
	0.121040	0.863(11)	−0.2066(46)	0.8597(81)	−0.2109(29)	−0.2043(25)	0.8815(63)
	0.121099	0.875(12)	−0.2142(66)	0.8692(70)	−0.2222(14)	−0.2103(24)	0.8988(33)
5.65	0.122005	0.8738(65)	−0.2145(25)	0.8738(65)	−0.2145(25)	−0.2145(25)	0.8738(65)
	0.122078	0.8861(62)	−0.2050(34)	0.8812(54)	−0.2124(26)	−0.2030(26)	0.9043(51)
	0.122130	0.815(34)	−0.192(14)	0.811(17)	−0.2104(76)	−0.1989(95)	0.8677(96)
	0.122167	0.8609(84)	−0.2078(78)	0.8513(62)	−0.2206(19)	−0.2008(41)	0.9034(44)
	0.122197	0.868(71)	−0.197(19)	0.821(72)	−0.206(22)	−0.198(13)	0.913(58)
5.80	0.122810	0.866(13)	−0.2062(55)	0.866(13)	−0.2062(55)	−0.2062(55)	0.866(13)
	0.122880	0.8543(55)	−0.2059(31)	0.8503(53)	−0.2062(54)	−0.1994(34)	0.8835(51)
	0.122940	0.848(11)	−0.1963(57)	0.8399(74)	−0.2155(55)	−0.1943(27)	0.9043(50)
5.95	0.123411	0.8649(47)	−0.2058(28)	0.8696(54)	−0.2019(51)	−0.2082(41)	0.8517(92)
	0.123460	0.828(21)	−0.197(15)	0.828(21)	−0.197(15)	−0.197(15)	0.828(21)
	0.123523	0.8522(70)	−0.2041(38)	0.8502(61)	−0.2112(23)	−0.2005(27)	0.8897(47)

TABLE IX. Table of the bare results for the individual quark contributions to the overall axial charge in the nucleon, Σ and Ξ baryons.

β	κ_l	$g^u_{A_P}$	$g^d_{A_P}$	$g^u_{A_\Sigma}$	$g^s_{A_\Sigma}$	$g^u_{A_\Xi}$	$g^s_{A_\Xi}$
5.40	0.119930	1.025(24)	−0.360(22)	1.025(24)	−0.360(22)	−0.360(22)	1.025(24)
	0.119989	1.024(26)	−0.344(20)	1.018(21)	−0.333(16)	−0.324(18)	1.0421(15)
	0.120048	1.019(48)	−0.322(32)	0.982(39)	−0.338(21)	−0.312(15)	1.031(18)
	0.120084	1.028(35)	−0.334(35)	0.983(53)	−0.340(10)	−0.316(12)	1.065(10)
5.50	0.120900	1.002(36)	−0.306(58)	1.002(36)	−0.306(58)	−0.306(58)	1.002(36)
	0.121040	0.959(74)	−0.306(58)	0.943(49)	−0.302(29)	−0.315(30)	1.035(24)
	0.121095	1.014(52)	−0.399(43)	0.978(21)	−0.3155(94)	−0.2930(90)	1.0445(72)
5.50	0.120950	1.009(49)	−0.298(24)	1.009(49)	−0.298(24)	−0.298(24)	1.009(49)
	0.121040	0.835(91)	−0.343(47)	0.913(45)	−0.309(20)	−0.299(23)	1.017(28)
	0.121099	0.964(88)	−0.341(41)	0.907(62)	−0.292(30)	−0.306(21)	1.021(24)
5.65	0.122005	0.950(48)	−0.294(34)	0.950(48)	−0.294(34)	−0.294(34)	0.950(48)
	0.122078	1.045(70)	−0.322(26)	1.046(57)	−0.317(19)	−0.295(18)	1.044(41)
	0.122130	0.973(91)	−0.319(31)	0.979(91)	−0.330(17)	−0.287(18)	1.070(24)
	0.122167	1.113(93)	−0.287(59)	1.024(42)	−0.310(17)	−0.282(13)	1.064(14)
	0.122197	1.049(59)	−0.335(76)	1.020(42)	−0.316(18)	−0.257(22)	1.107(16)

(Table continued)

TABLE IX. *(Continued)*

β	κ_l	$g^u_{A_P}$	$g^d_{A_P}$	$g^u_{A_\Sigma}$	$g^s_{A_\Sigma}$	$g^u_{A_\Xi}$	$g^s_{A_\Xi}$
5.80	0.122810	0.966(63)	−0.223(35)	0.966(63)	−0.223(35)	−0.223(35)	0.966(63)
	0.122880	1.042(56)	−0.336(25)	1.032(46)	−0.333(15)	−0.309(61)	1.041(21)
	0.122940	1.028(71)	−0.326(35)	0.987(86)	−0.295(38)	−0.296(25)	1.028(35)
5.95	0.123411	0.975(33)	−0.294(18)	0.967(40)	−0.270(38)	−0.308(32)	0.941(56)
	0.123460	0.992(41)	−0.308(22)	0.992(41)	−0.308(22)	−0.308(22)	0.992(41)
	0.123523	1.035(94)	−0.364(62)	1.004(63)	−0.340(34)	−0.302(36)	0.960(56)

TABLE X. Table of the bare results for the individual quark contributions to the overall scalar charge in the nucleon, Σ and Ξ baryons.

β	κ_l	$g^u_{S_P}$	$g^d_{S_P}$	$g^u_{S_\Sigma}$	$g^s_{S_\Sigma}$	$g^u_{S_\Xi}$	$g^s_{S_\Xi}$
5.40	0.119930	4.34(11)	2.854(77)	4.34(11)	2.854(77)	2.854(77)	4.34(11)
	0.119989	4.32(14)	2.987(92)	4.03(12)	2.695(46)	2.683(71)	4.181(66)
	0.120048	4.44(41)	3.28(18)	3.98(15)	2.467(91)	3.01(22)	4.43(13)
	0.120084	4.29(64)	2.62(47)	4.04(20)	2.702(42)	2.633(90)	4.282(50)
5.50	0.120900	4.26(10)	2.766(74)	4.26(10)	2.766(74)	2.766(74)	4.26(10)
	0.121040	4.93(43)	3.41(24)	4.35(25)	2.642(60)	2.73(10)	4.201(70)
	0.121095	5.60(29)	4.13(23)	4.10(19)	2.514(34)	2.474(93)	4.028(39)
5.50	0.120950	4.209(16)	2.81(11)	4.209(16)	2.81(11)	2.81(11)	4.209(16)
	0.121040	5.39(36)	3.83(29)	4.31(21)	2.867(59)	2.77(14)	4.388(87)
	0.121099	5.50(52)	4.46(41)	5.44(59)	2.937(68)	3.09(26)	4.611(94)
5.65	0.122005	4.83(23)	3.15(13)	4.83(23)	3.15(13)	3.15(13)	4.83(23)
	0.122078	4.78(20)	3.163(19)	4.16(13)	2.705(51)	2.82(13)	4.53(10)
	0.122130	5.21(55)	4.02(53)	4.31(25)	2.663(56)	2.55(14)	4.242(63)
	0.122167	5.73(39)	4.15(22)	4.01(23)	2.759(46)	2.61(13)	4.344(70)
	0.122197	6.34(59)	4.36(40)	4.04(38)	2.755(75)	2.50(21)	4.279(92)
5.80	0.122810	4.47(27)	2.89(16)	4.47(27)	2.89(16)	2.89(16)	4.47(27)
	0.122880	4.55(20)	3.34(13)	3.96(15)	2.937(73)	2.76(10)	4.43(10)
	0.122940	5.26(68)	4.15(73)	4.20(33)	2.872(70)	2.61(23)	4.384(90)
5.95	0.123411	4.18(34)	2.82(22)	5.00(28)	3.84(63)	3.39(17)	5.56(64)
	0.123460	5.21(27)	3.38(17)	5.21(27)	3.38(17)	3.38(17)	5.21(27)
	0.123523	4.84(28)	3.57(23)	4.24(24)	2.901(90)	2.93(18)	4.29(10)

APPENDIX C: HYPERON MATRIX ELEMENTS

Reconstruction of the hyperon matrix elements as shown to first order in Ref. [55] and given to second order here:

$$\begin{aligned}
\langle\Sigma^+|\bar{u}\Gamma u|\Sigma^+\rangle &= 2\sqrt{2}f + (-2\sqrt{2}s_1 + \sqrt{6}s_2)\delta m_l + \sqrt{2}f_3\delta m_l^2,\\
\langle\Sigma^+|\bar{s}\Gamma s|\Sigma^+\rangle &= \sqrt{2}(f-\sqrt{3}d) + \left(-\sqrt{\frac{3}{2}}r_1 - 3\sqrt{2}r_3 - \sqrt{2}s_1 + \sqrt{\frac{3}{2}}s_2\right)\delta m_l + \left(-\sqrt{\frac{3}{2}}d_2 + \frac{1}{\sqrt{2}}f_3\right)\delta m_l^2,\\
\langle\Xi^0|\bar{u}\Gamma u|\Xi^0\rangle &= \sqrt{2}(f-\sqrt{3}d) + (2\sqrt{2}r_3 + 2\sqrt{2}s_1)\delta m_l + \left(-\sqrt{\frac{3}{2}}d_4 + \frac{1}{\sqrt{2}}f_2\right)\delta m_l^2,\\
\langle\Xi^0|\bar{u}\Gamma u|\Xi^0\rangle &= \sqrt{2}(f-\sqrt{3}d) + (2\sqrt{2}r_3 + 2\sqrt{2}s_1)\delta m_l + \left(-\sqrt{\frac{3}{2}}d_4 + \frac{1}{\sqrt{2}}f_2\right)\delta m_l^2.
\end{aligned} \tag{C1}$$

[1] P. Zyla *et al.* (Particle Data Group), Review of particle physics, Prog. Theor. Exp. Phys. **2020**, 083C01 (2020), and 2021 update.

[2] J. D. Jackson, S. B. Treiman, and H. W. Wyld, Possible tests of time reversal invariance in beta decay, Phys. Rev. **106**, 517 (1957).

[3] W. Wilburn, V. Cirigliano, A. Klein, M. Makela, P. McGaughey, C. Morris, J. Ramsey, A. Salas-Bacci, A. Saunders, L. Brousard, and A. Young, Measurement of the neutrino-spin correlation parameter b in neutron decay using ultracold neutrons, Rev. Mex. Fis. **55**, 119 (2009).

[4] D. Počanić *et al.*, Nab: Measurement principles, apparatus and uncertainties, Nucl. Instrum. Methods Phys. Res., Sect. A **611**, 211 (2009).

[5] X. Sun *et al.*, Improved limits on Fierz interference using asymmetry measurements from the ultracold neutron asymmetry (UCNA) experiment, Phys. Rev. C **101**, 035503 (2020).

[6] T. Bhattacharya, V. Cirigliano, S. D. Cohen, A. Filipuzzi, M. Gonzalez-Alonso, M. L. Graesser, R. Gupta, and H.-W. Lin, Probing novel scalar and tensor interactions from (ultra) cold neutrons to the LHC, Phys. Rev. D **85**, 054512 (2012).

[7] M. Aaboud, G. Aad, B. Abbott *et al.*, Search for a new heavy gauge-boson resonance decaying into a lepton and missing transverse momentum in 36 fb^{-1} of pp collisions at $\sqrt{s} = 13$ TeV with the ATLAS experiment, Eur. Phys. J. C **78**, 401 (2018).

[8] M. Pospelov and A. Ritz, Electric dipole moments as probes of new physics, Ann. Phys. (Amsterdam) **318**, 119 (2005).

[9] J. R. Ellis and R. A. Flores, Implications of the strange spin of the nucleon for the neutron electric dipole moment in supersymmetric theories, Phys. Lett. B **377**, 83 (1996).

[10] T. Bhattacharya, V. Cirigliano, S. D. Cohen, R. Gupta, A. Joseph, H.-W. Lin, and B. Yoon, Iso-vector and iso-scalar tensor charges of the nucleon from lattice QCD, Phys. Rev. D **92**, 094511 (2015).

[11] M. Pitschmann, C.-Y. Seng, C. D. Roberts, and S. M. Schmidt, Nucleon tensor charges and electric dipole moments, Phys. Rev. D **91**, 074004 (2015).

[12] C. Abel *et al.*, Measurement of the permanent electric dipole moment of the neutron, Phys. Rev. Lett. **124**, 081803 (2020).

[13] R. Gupta, Y.-C. Jang, B. Yoon, H.-W. Lin, V. Cirigliano, and T. Bhattacharya (Precision Neutron Decay Matrix Elements (PNDME) Collaboration), Isovector charges of the nucleon from $2+1+1$-flavor lattice QCD, Phys. Rev. D **98**, 034503 (2018).

[14] C. C. Chang *et al.*, A per-cent-level determination of the nucleon axial coupling from quantum chromodynamics, Nature (London) **558**, 91 (2018).

[15] J. Liang, Y.-B. Yang, T. Draper, M. Gong, and K.-F. Liu (χQCD Collaboration), Quark spins and anomalous ward identity, Phys. Rev. D **98**, 074505 (2018).

[16] A. Walker-Loud, E. Berkowitz, D. Brantley, A. S. Gambhir, P. Vranas, C. Bouchard, M. Clark, C. C. Chang, N. Garron, B. Joo, T. Kurth, H. Monge-Camacho, A. Nicholson, C. Monahan, K. Orginos, and E. Rinaldi, Lattice QCD determination of the nucleon axial charge, Proc. Sci. CD2018 (**2020**) 020 [arXiv:1912.08321].

[17] T. Harris, G. von Hippel, P. Junnarkar, H. B. Meyer, K. Ottnad, J. Wilhelm, H. Wittig, and L. Wrang, Nucleon isovector charges and twist-2 matrix elements with $N_f = 2+1$ dynamical wilson quarks, Phys. Rev. D **100**, 034513 (2019).

[18] G. S. Bali, S. Collins, B. Gläßle, M. Göckeler, J. Najjar, R. H. Rödl, A. Schäfer, R. W. Schiel, W. Söldner, and A. Sternbeck (RQCD Collaboration), Nucleon isovector couplings from $N_f = 2$ lattice QCD, Phys. Rev. D **91**, 054501 (2015).

[19] J. He, D. A. Brantley, C. C. Chang, I. Chernyshev, E. Berkowitz, D. Howarth, C. Körber, A. S. Meyer, H. Monge-Camacho, E. Rinaldi, C. Bouchard, M. A. Clark, A. S. Gambhir, C. J. Monahan, A. Nicholson, P. Vranas, and A. Walker-Loud, Detailed analysis of excited-state systematics in a lattice QCD calculation of g_A, Phys. Rev. C **105**, 065203 (2022).

[20] A. J. Chambers, R. Horsley, Y. Nakamura, H. Perlt, D. Pleiter, P. E. L. Rakow, G. Schierholz, A. Schiller, H. Stüben, R. D. Young, and J. M. Zanotti, Feynman-Hellmann approach to the spin structure of hadrons, Phys. Rev. D **90**, 014510 (2014).

[21] A. Chambers, R. Horsley, Y. Nakamura, H. Perlt, P. Rakow, G. Schierholz, A. Schiller, and J. Zanotti, A novel approach to nonperturbative renormalization of singlet and nonsinglet lattice operators, Phys. Lett. B **740**, 30 (2015).

[22] A. J. Chambers, R. Horsley, Y. Nakamura, H. Perlt, D. Pleiter, P. E. L. Rakow, G. Schierholz, A. Schiller, H. Stüben, R. D. Young, and J. M. Zanotti, Disconnected contributions to the spin of the nucleon, Phys. Rev. D **92**, 114517 (2015).

[23] R. Horsley, Y. Nakamura, H. Perlt, D. Pleiter, P. E. L. Rakow, G. Schierholz, A. Schiller, H. Stüben, R. D. Young, and J. M. Zanotti, The strange quark contribution to the spin of the nucleon, Proc. Sci. LATTICE2018 (**2018**) 119 [arXiv:1901.04792].

[24] R. Horsley, R. Millo, Y. Nakamura, H. Perlt, D. Pleiter, P. Rakow, G. Schierholz, A. Schiller, F. Winter, and J. Zanotti, A lattice study of the glue in the nucleon, Phys. Lett. B **714**, 312 (2012).

[25] A. J. Chambers, R. Horsley, Y. Nakamura, H. Perlt, P. E. L. Rakow, G. Schierholz, A. Schiller, K. Somfleth, R. D. Young, and J. M. Zanotti, Nucleon structure functions from operator product expansion on the lattice, Phys. Rev. Lett. **118**, 242001 (2017).

[26] K. U. Can *et al.*, Lattice QCD evaluation of the Compton amplitude employing the Feynman-Hellmann theorem, Phys. Rev. D **102**, 114505 (2020).

[27] A. Hannaford-Gunn, K. U. Can, R. Horsley, Y. Nakamura, H. Perlt, P. E. L. Rakow, G. Schierholz, H. Stüben, R. D. Young, and J. M. Zanotti (CSSM/QCDSF/UKQCD Collaborations), Generalized parton distributions from the off-forward Compton amplitude in lattice QCD, Phys. Rev. D **105**, 014502 (2022).

[28] N. Cundy, M. Göckeler, R. Horsley, T. Kaltenbrunner, A. D. Kennedy, Y. Nakamura, H. Perlt, D. Pleiter, P. E. L. Rakow, A. Schäfer, G. Schierholz, A. Schiller, H. Stüben, and J. M. Zanotti (QCDSF-UKQCD Collaboration), Nonperturbative improvement of stout-smeared three-flavor clover fermions, Phys. Rev. D **79**, 094507 (2009).

[29] W. Bietenholz, V. Bornyakov, N. Cundy, M. Göckeler, R. Horsley, A. Kennedy, W. Lockhart, Y. Nakamura, H. Perlt, D. Pleiter, P. Rakow, A. Schäfer, G. Schierholz, A. Schiller, H. Stüben, and J. Zanotti, Tuning the strange quark mass in lattice simulations, Phys. Lett. B **690**, 436 (2010).

[30] V. Bornyakov, R. Horsley, R. J. Hudspith, Y. Nakamura, H. Perlt, D. Pleiter, P. E. L. Rakow, G. Schierholz, A. Schiller, H. Stuben, and J. M. Zanotti, Wilson flow and scale setting from lattice QCD, arXiv:1508.05916.

[31] M. Constantinou, R. Horsley, H. Panagopoulos, H. Perlt, P. E. L. Rakow, G. Schierholz, A. Schiller, and J. M. Zanotti, Renormalization of local quark-bilinear operators for $N_f = 3$ flavors of stout link nonperturbative clover fermions, Phys. Rev. D **91**, 014502 (2015).

[32] J. Bickerton, Transverse properties of baryons using lattice quantum chromodynamics, The University of Adelaide, https://hdl.handle.net/2440/129589 (2020).

[33] S. Capitani, M. Göckeler, R. Horsley, H. Perlt, D. Petters, D. Pleiter, P. Rakow, G. Schierholz, A. Schiller, and P. Stephenson, Towards a lattice calculation of Δq and δq, Nucl. Phys. B, Proc. Suppl. **79**, 548 (1999).

[34] B. Blossier, M. D. Morte, G. von Hippel, T. Mendes, and R. Sommer (ALPHA Collaboration), On the generalized eigenvalue method for energies and matrix elements in lattice field theory, J. High Energy Phys. 04 (2009) 094.

[35] G. P. Engel, C. B. Lang, M. Limmer, D. Mohler, and A. Schäfer (BGR [Bern-Graz-Regensburg] Collaboration), Meson and baryon spectrum for QCD with two light dynamical quarks, Phys. Rev. D **82**, 034505 (2010).

[36] M. S. Mahbub, W. Kamleh, D. B. Leinweber, P. J. Moran, and A. G. Williams, Roper resonance in $2 + 1$ flavor QCD, Phys. Lett. B **707**, 389 (2012).

[37] A. L. Kiratidis, W. Kamleh, D. B. Leinweber, and B. J. Owen, Lattice baryon spectroscopy with multiparticle interpolators, Phys. Rev. D **91**, 094509 (2015).

[38] M. S. Mahbub, W. Kamleh, D. B. Leinweber, P. J. Moran, and A. G. Williams, Structure and flow of the nucleon eigenstates in lattice QCD, Phys. Rev. D **87**, 094506 (2013).

[39] B. J. Menadue, W. Kamleh, D. B. Leinweber, and M. S. Mahbub, Isolating the $\Lambda(1405)$ in lattice QCD, Phys. Rev. Lett. **108**, 112001 (2012).

[40] R. G. Edwards, J. J. Dudek, D. G. Richards, and S. J. Wallace, Excited state baryon spectroscopy from lattice QCD, Phys. Rev. D **84**, 074508 (2011).

[41] B. J. Owen, W. Kamleh, D. B. Leinweber, M. S. Mahbub, and B. J. Menadue, Transition of $\rho \to \pi\gamma$ in lattice QCD, Phys. Rev. D **92**, 034513 (2015).

[42] J. M. M. Hall, W. Kamleh, D. B. Leinweber, B. J. Menadue, B. J. Owen, A. W. Thomas, and R. D. Young, Lattice QCD evidence that the $\Lambda(1405)$ resonance is an antikaon-nucleon molecule, Phys. Rev. Lett. **114**, 132002 (2015).

[43] B. J. Owen, W. Kamleh, D. B. Leinweber, M. S. Mahbub, and B. J. Menadue, Light meson form factors at near physical masses, Phys. Rev. D **91**, 074503 (2015).

[44] B. J. Owen, J. Dragos, W. Kamleh, D. B. Leinweber, M. S. Mahbub, B. J. Menadue, and J. M. Zanotti, Variational approach to the calculation of g_A, Phys. Lett. B **723**, 217 (2013).

[45] H.-W. Lin, S. D. Cohen, R. G. Edwards, and D. G. Richards, Lattice study of the $n - P_{11}$ transition form factors, Phys. Rev. D **78**, 114508 (2008).

[46] B. Yoon, R. Gupta, T. Bhattacharya, M. Engelhardt, J. Green, B. Joó, H.-W. Lin, J. Negele, K. Orginos, A. Pochinsky, D. Richards, S. Syritsyn, and F. Winter (Nucleon Matrix Elements (NME) Collaboration), Controlling excited-state contamination in nucleon matrix elements, Phys. Rev. D **93**, 114506 (2016).

[47] S. Dinter, C. Alexandrou, M. Constantinou, V. Drach, K. Jansen, and D. B. Renner, Precision study of excited state effects in nucleon matrix elements, Phys. Lett. B **704**, 89 (2011).

[48] T. Bhattacharya, S. D. Cohen, R. Gupta, A. Joseph, H.-W. Lin, and B. Yoon, Nucleon charges and electromagnetic form factors from $2 + 1 + 1$-flavor lattice QCD, Phys. Rev. D **89**, 094502 (2014).

[49] S. Capitani, M. Della Morte, D. Djukanovic, G. von Hippel, J. Hua, B. Jäger, B. Knippschild, H. B. Meyer, T. D. Rae, and H. Wittig, Nucleon electromagnetic form factors in two-flavor QCD, Phys. Rev. D **92**, 054511 (2015).

[50] J. R. Green, J. W. Negele, A. V. Pochinsky, S. N. Syritsyn, M. Engelhardt, and S. Krieg, Nucleon electromagnetic form factors from lattice QCD using a nearly physical pion mass, Phys. Rev. D **90**, 074507 (2014).

[51] S. Capitani, M. Della Morte, G. von Hippel, B. Jäger, A. Jüttner, B. Knippschild, H. B. Meyer, and H. Wittig, Nucleon axial charge in lattice QCD with controlled errors, Phys. Rev. D **86**, 074502 (2012).

[52] J. Dragos, R. Horsley, W. Kamleh, D. B. Leinweber, Y. Nakamura, P. E. L. Rakow, G. Schierholz, R. D. Young, and J. M. Zanotti, Nucleon matrix elements using the variational method in lattice QCD, Phys. Rev. D **94**, 074505 (2016).

[53] S. R. Beane, W. Detmold, R. Horsley, M. Illa, M. Jafry, D. J. Murphy, Y. Nakamura, H. Perlt, P. E. L. Rakow, G. Schierholz, P. E. Shanahan, H. Stüben, M. L. Wagman, F. Winter, R. D. Young, and J. M. Zanotti (NPLQCD and QCDSF Collaborations), Charged multihadron systems in lattice QCD + QED, Phys. Rev. D **103**, 054504 (2021).

[54] E. Rinaldi, S. Syritsyn, M. L. Wagman, M. I. Buchoff, C. Schroeder, and J. Wasem, Lattice QCD determination of neutron-antineutron matrix elements with physical quark masses, Phys. Rev. D **99**, 074510 (2019).

[55] J. M. Bickerton, R. Horsley, Y. Nakamura, H. Perlt, D. Pleiter, P. E. L. Rakow, G. Schierholz, H. Stüben, R. D. Young, and J. M. Zanotti, Patterns of flavor symmetry breaking in hadron matrix elements involving u, d, and s quarks, Phys. Rev. D **100**, 114516 (2019).

[56] W. Bietenholz, V. Bornyakov, M. Göckeler, R. Horsley, W. G. Lockhart, Y. Nakamura, H. Perlt, D. Pleiter, P. E. L. Rakow, G. Schierholz, A. Schiller, T. Streuer, H. Stüben, F. Winter, and J. M. Zanotti (QCDSF-UKQCD Collaboration), Flavor blindness and patterns of flavor symmetry breaking in lattice simulations of up, down, and strange quarks, Phys. Rev. D **84**, 054509 (2011).

[57] S. R. Beane and M. J. Savage, Baryon axial charge in a finite volume, Phys. Rev. D **70**, 074029 (2004).

[58] J. Bickerton, A. Cooke, R. Horsley, Y. Nakamura, H. Perlt, D. Pleiter, P. Rakow, G. Schierholz, H. Stüben, R. Young, and J. Zanotti, Patterns of flavour symmetry breaking in

hadron matrix elements involving u, d and s quarks, Proc. Sci. LATTICE2021 (**2022**) 490 [arXiv:2112.04445].
[59] Y. Aoki, T. Blum, G. Colangelo, S. Collins, M. Della Morte, P. Dimopoulos, S. Dürr, X. Feng, H. Fukaya, M. Golterman *et al.*, Flag review 2021, Eur. Phys. J. C **82**, 869 (2022).
[60] H. Akaike, On the likelihood of a time series model, J. R. Stat. Soc. D (Statistician) **27**, 217 (1978).
[61] H.-M. Chang, M. González-Alonso, and J. Martin Camalich, Nonstandard semileptonic hyperon decays, Phys. Rev. Lett. **114**, 161802 (2015).
[62] J. C. Hardy and I. S. Towner, Superallowed $0^+ \to 0^+$ nuclear β decays: A new survey with precision tests of the conserved vector current hypothesis and the standard model, Phys. Rev. C **79**, 055502 (2009).
[63] M. Bychkov, D. Počanić, B. A. VanDevender, V. A. Baranov, W. Bertl *et al.*, New precise measurement of the pion weak form factors in $\pi^+ \to e^+\nu\gamma$ decay, Phys. Rev. Lett. **103**, 051802 (2009).
[64] R. Gupta, B. Yoon, T. Bhattacharya, V. Cirigliano, Y.-C. Jang, and H.-W. Lin (PNDME Collaboration), Flavor diagonal tensor charges of the nucleon from $(2 + 1 + 1)$-flavor lattice QCD, Phys. Rev. D **98**, 091501 (2018).
[65] T. Haar, Y. Nakamura, and H. Stüben, An update on the BQCD hybrid Monte Carlo program, EPJ Web Conf. **175** (2017).
[66] R. G. Edwards and B. Joo, The Chroma software system for lattice QCD, Nucl. Phys. B, Proc. Suppl. **140**, 832 (2005).